

The study of laser deep penetration processing on prefabricated cracks of high carbon steel

Dongwei Liu

Changchun University of Science and Technology

Yan Shi (✉ shiyang1972@126.com)

Changchun University of Science and Technology

Jia Liu

Changchun University of Science and Technology

Original Article

Keywords: laser deep penetration processing, high carbon steel, fragmentation

Posted Date: November 13th, 2020

DOI: <https://doi.org/10.21203/rs.3.rs-106439/v1>

License: © ⓘ This work is licensed under a Creative Commons Attribution 4.0 International License.

[Read Full License](#)

Version of Record: A version of this preprint was published at Optics & Laser Technology on December 1st, 2021. See the published version at <https://doi.org/10.1016/j.optlastec.2021.107414>.

The study of laser deep penetration processing on prefabricated cracks of high carbon steel

Dongwei Liu ^{a, b}, Yan Shi ^{a, b, *}, Jia Liu ^{a, b}

^a School of Mechanical and Electric Engineering, Changchun University of Science and Technology, Changchun130022, P. R. China

^b National Base of International Science and Technology Cooperation for Optics, Changchun130022, P. R. China

Abstract:

This paper describes the testing of laser deep penetration processing on controlled fragmentation of high carbon steel (50SiMnVB). The objective of this research is to make use of defects in deep penetration zones and optimize the quality of prefabricated cracks. The research shows that a deeper central crack appear in the deep penetration zone when the heat input is 60 J/mm, and the appeared crack is affected by martensite in microstructure, high microhardness and a high magnitude of tensile stress. Furthermore, the fracture mode of the deep penetration zones is mixed-mode (ductile and brittle fracture).

Keywords: laser deep penetration processing; high carbon steel; fragmentation

1. Introduction

It is known that 50SiMnVB steel has many excellent properties such as higher fragment rate and superior hardness. It is contributed to higher content of carbon, silicon and manganese elements [1]. Thus, it is utilized widely in various fields such as the projectile materials [2].

Nowadays, many pre-controlled fragment technologies have emerged. For instance, a main traditional pre-controlled fragment technology is machining grooves [3-5]. However, in order to maintain the cutting accuracy, it is necessary to service the cutting tool frequently. Thus, the cutting efficiency may decrease greatly [6]. Currently, laser has been proven to be an innovative tool in the field of pre-controlled fragment [7]. The processing methods include deep laser melting [4], laser transformation notching [6], laser cutting [8, 9], laser microdrilling [10, 11], and laser scribing [12]. They make the modified zones more brittle and micro-cracks tend to form macro cracks with the plastic deformation in the case of higher tensile stresses [4, 6, 13].

Although the laser pre-controlled fragment technologies have many advantages that machining grooves do not have, there are still many problems to be solved. For instance, Liu et al. [14] pointed out that the transformation hardening appeared in the

* Corresponding author.

Address: School of Mechanical and Electric Engineering, Changchun University of Science and Technology, No.7089 Weixing Road, Changchun 130022, P. R. China. Tel: +86-431-85582207.
E-mail address: shiyan@cust.edu.cn

modified zones because of the martensite after laser processing. However, there are not any obvious cracks. In 2013, Villano reported the availability of deep laser melting and laser microdrilling [4]. Similarly, cracks rarely appeared. The effect of laser transformation notching on the controlled fracture was investigated by Zhang et al. [6]. Although they found that there were many cracks in the modified zones, the depth and quality of the cracks are not satisfactory.

This paper elaborates on the study of laser deep penetration processing (LDPP) on controlled fragmentation of high carbon steel. The objective of this research is to make use of defect in deep penetration zones and optimize the quality of prefabricated cracks. Moreover, we also explore the relationship between the heat input and the degree of cracking in the deep penetration zones. Finally, we reveal the fracture mechanism through the fracture morphology analysis combining numerical simulation. In a certain sense, this paper has a significant guidance to the fracture mechanism by laser deep penetration processing, and this processing have a potential application in pre-controlled fragment.

2. Material and methods

2.1 Materials

The chemical composition of 50SiMnVB steel is shown in **Table 1**. Test specimens of 120 × 120 mm were cut by applying electrospark wire-electrode cutting (WEDM) at a 14-mm thickness. Then, they were grounded mechanically using SiC papers and in order to eliminate the contaminants that adhere to the surface of the specimens, the specimens were wiped with industrial alcohol, followed by drying with an air dryer. In addition, the quenching and tempering treatment were developed over the specimens in order to strengthen the performance (especially strength and microstructure). The purpose of operation is to eliminate the cracks error caused by inhomogeneity in the structure. The heat treatment parameters is shown in **Table 2** [15].

Table 1 Chemical composition of 50SiMnVB steel (wt. %).

Composition	C	Si	Mn	Cr	V	B
Percent (wt. %)	0.46~0.52	1.35~1.70	1.35~1.70	0.15~0.35	0.02~0.06	0.0005~0.0035

Table 2 Heat treatment parameters of 50SiMnVB steel.

	Quenching	Tempering
Heating temperature/°C	840~880	400~500
Cooling way	Oil cooling	Air cooling

2.2 Laser deep penetration processing

The test specimens were LDPP (the continuous wave laser processing) by an automatic welding system composed of two parts: an HL4006D solid-state laser and a KR30/HA six-axis linkage robot. The optical configuration consists of the reflector

and the reflection focusing mirror. The parameters about laser deep penetration processing is shown in **Table 3**. Moreover, according to the preliminary test in **Table 4**, we chose four groups of laser process parameters for specimens to be analyzed and they are indicated in **Table 5**. Then, we intercepted the specimens using the WEDM after accomplishing the laser process. They are prepared into samples for the following series of experiments by grinding and polishing with SiC paper and a slurry of alumina powder, respectively. Finally, the metallographic specimens are etched by adopting 4% nital. The heat input (HI) can be described with the following formula [16]:

$$HI = E = \frac{P}{v} \quad (1)$$

where P is the laser power; v is the scanning speed; and E is the laser line energy. A schematic diagram of the LDPP is shown in **Fig. 1**.

Table 3 Parameters about laser deep penetration processing.

Collimated beam size (mm)	Defocus (mm)	beam quality factor	Shielding gas	Protective gas flow (L/min)
0.3	0	>0.9	Argon	20~25

Table 4 A preliminary test in vary the laser power and scanning speed. ‘×’ stands for a central crack appearing in deep penetration zone, ‘√’ stands for there is no central crack appearing. The yellow areas stand for the parameters selected in this research.

Laser power (kw)	Scanning speed (m/min)							
	1.0	1.5	2.0	2.5	3.0	3.5	4.0	4.5
1.0	×	×	×	×	×	×	×	×
2.0	√	√	√	√	√	√	√	×
3.0	√	√	√	√	√	√	√	√
4.0	×	×	×	×	√	√	√	√

Table 5 Data of the main features of the deep penetration zones. Among them, the depth and width are the average values (three times) obtained from the different cross sections. The measured results are all within the error range.

numbering	Laser power (kW)	Scanning speed (m/min)	Heat input (J/mm)	Depth (mm)	Width (mm)	The ratio of depth to width	cracking
L-1	2.0	4.5	27	1.923	1.692	1.137	No
L-2	3.0	3.5	51	3.385	1.692	2.001	Yes
L-3	3.0	3.0	60	4.385	1.923	2.280	Yes
L-4	4.0	1.0	240	9.231	3.923	2.353	No

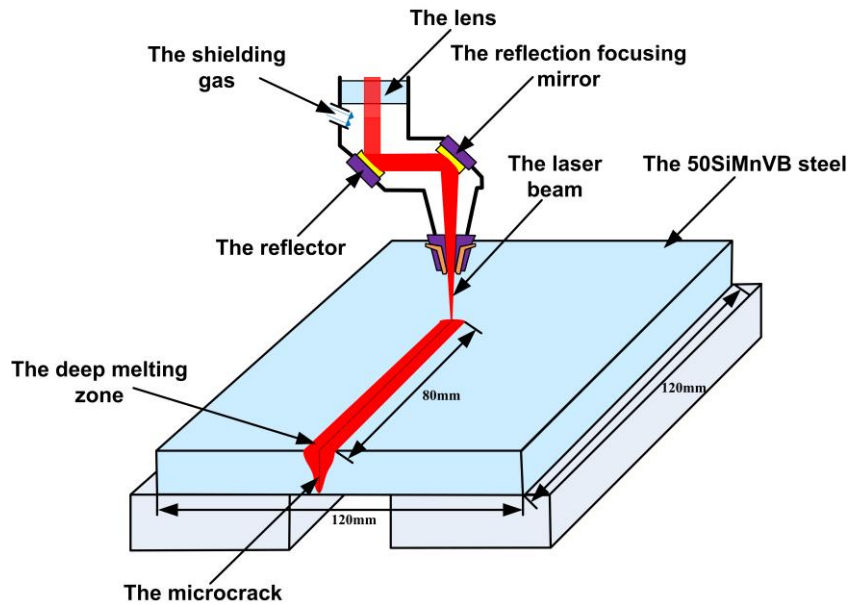


Fig. 1 Schematic representation of laser deep penetration processing.

2.3 Microhardness

The cross-section of the microhardness was determined using MH-60 microhardness tester. The loading time and the load mass were set to 10s and 200g, respectively. The micro indentation was used for microhardness evaluation. And in order to eliminate indentation size effect as much as possible, the test force (load mass) was maximized within the allowable range.

2.4 Microstructural analysis

A scanning electron microscope (SEM) and optical microscope (OM) were used to observe the microstructure and fracture morphology, respectively. The models of SEM and OM were JSM-6510F and LeiCaDM2700M, respectively. In this study, a microstructural analysis was conducted by taking a cross section of the specimens. The fracture morphology is sampled from specimens using WEDM. A schematic is shown in **Fig. 2**.

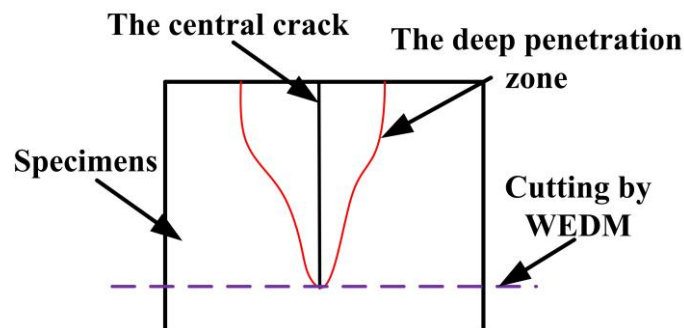


Fig. 2 A schematic of sampling fracture morphology.

2.5 Numerical simulation analysis

A temperature and stress field were determined by SYSWELD software. It is widely used in the simulation of welding process. The objective of numerical

simulation analysis is to reveal the mechanism of fracture and explore the process of dynamic response.

3. Results and discussion

3.1 Macroscopic morphology

As shown in **Table 5**, the depth and width in the deep penetration zones increase basically when the heat input (HI) increases. However, from **Fig. 3** (a) and (b), there is little difference in the melting width when HI are 27 J/mm, 51 J/mm and 60 J/mm. When HI is 240 J/mm, the depth increases obviously because the higher HI. The results are supported by Zheng et al. [10] and Gadallah et al. [17]. In 2013, Villano [4] made it clear that projectile bodies has a good fragmentation rate when the depth in external groove increase to 50% of the thickness of casing. In this research, the values of casing thickness and depth in L-4 are 14 mm and 9.231 mm, respectively. The result is supported by D. Villano. Moreover, **Fig. 3** (c) shows the schematic diagram of the the ratio of depth to width. It can be seen that the the ratio of depth to width increases when HI increases. It should be noted that the ratio of depth to width increases slowly when HI jumps from 60 J/mm to 240 J/mm. The ratio of depth to width is one of the most important parameters and it can provides a reference value for geometric regular fragments and damage ability.

More details of macro morphology are shown in **Fig. 4**. it can be seen that the position of cracks are controlled successfully (There are central cracks in image (b) and (c)). It's important to point out that various columnar crystals appear in region D in **Fig. 4** (e). There are many random oriented small crystals near the fusion zones and they grow rapidly into dendritic branches along the preferential direction in crystallography. They dominate the pattern of solid-liquid interface because of the faster growth in crystals that are parallel to the direction of the heat flow. Finally, the crystals with preferred orientation die out the others and a typical columnar crystal (region D) is formed [18]. Finally, the narrow gap (central crack) is created because of tensile stress caused by cooling and shrinkage. It will be further discussed in section 3.3 and 3.4.

In addition, from image (a) and (d) in **Fig. 4**, it can be seen that there are no cracks in DPZ when HI are 27 J/mm and 240 J/mm. However, it should be pointed out that central cracks appear in deep penetration zones when HI is moderate (51 J/mm and 60 J/mm), and the depth of crack corresponding to 60 J/mm is longer (4.385mm) than that of 51 J/mm (3.385mm). The identical conclusions were also obtained by Y.L. Hu et al. [19].

Furthermore, in **Fig. 4** (b) and (d), it can be seen that there are some defects in DPZ such as porosity (region A) and cavitation (region B). In LDPP, the unstable molten pool and fast cooling rate restrain gas escaping from the pools. Depending on the theory of F-R model [20], F-R dislocation sources can emit dislocation lines to

aggravate the degree of plastic deformation and the severe plastic deformation attacked micro-cracks when the dislocation density reaches a certain degree. Furthermore, micro-cracks clubbed together and prolonged the area of aggression under the effect of thermal stress. Although defects are usually bad for the performance in welding joints [21], it is profitable to the formation of pre-cracks in this research.

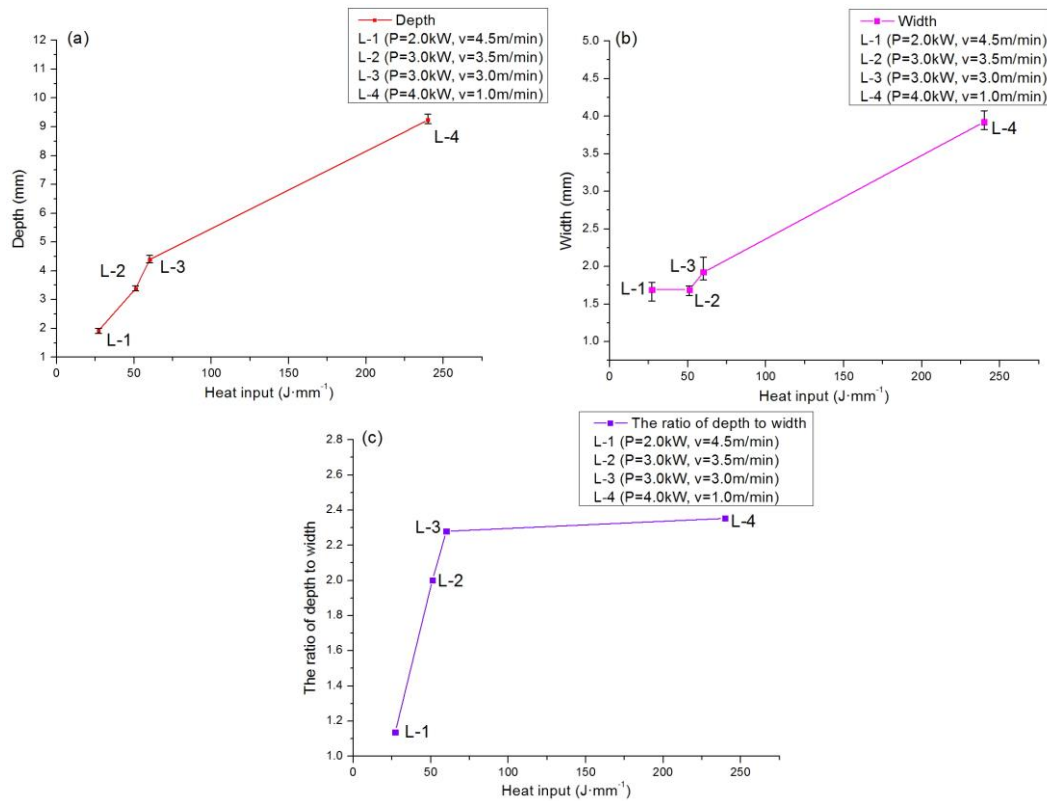
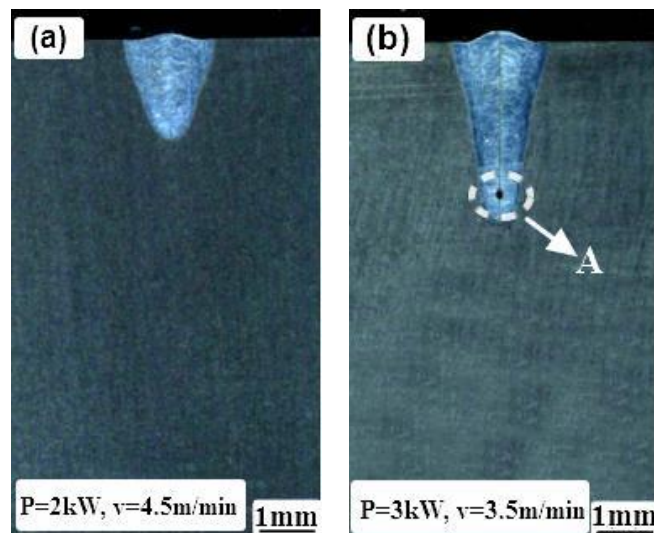


Fig. 3 Relationship among the depth, width, the ratio of depth to width and heat input. (a) relationship between the depth and heat input; (b) relationship between the width and heat input; (c) relationship between the ratio of depth to width and heat input.



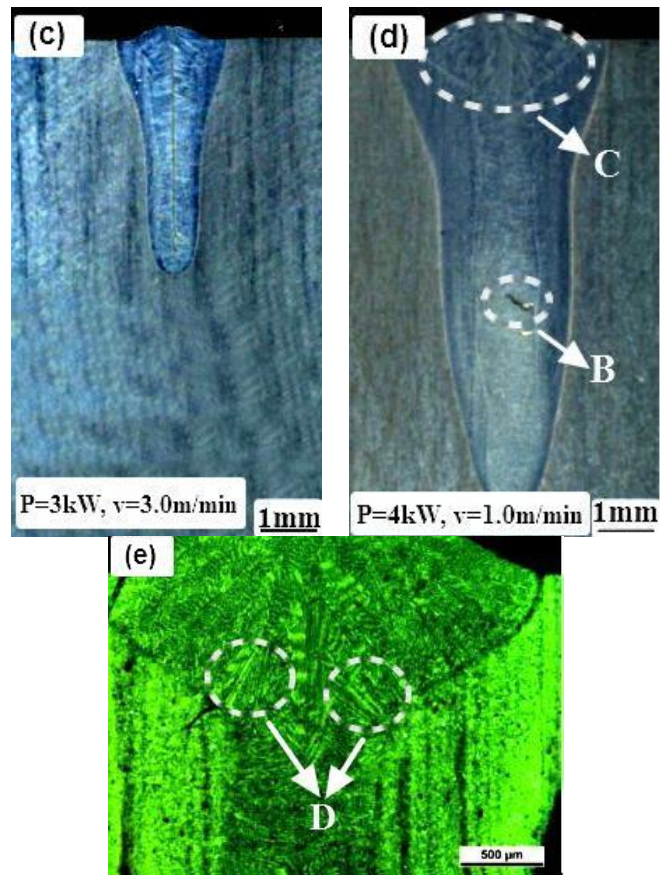


Fig. 4 OM examination of (a) L-1; (b) L-2; (c) L-3; (d) L-4; (e) magnify of region C.

3.2 Microstructure and microhardness

The macroscopic morphology of entire DPZ is shown in **Fig. 5** (a). The different zones from right to left are: base material (BM), heat affected zone (HAZ) and deep penetration zone (DPZ). As can be noted from image (b) to (d), massive lath martensite appears such as region A, C, and E. Region G is a typical martensite structure and it reveals the regular triangle. It is characterized by cluster and parallel arrangement. Moreover, the pattern of martensite is different from image (b) to (d) because the martensite existing in HAZ is smaller than the others. According to the thermodynamic theory of martensitic transformation [22], the elastic stress existing on semi-coherent interfaces decreases the potential energy of interface motion during the process of martensite growth, and then a high magnitude of driving force make the growth rate of martensites faster.

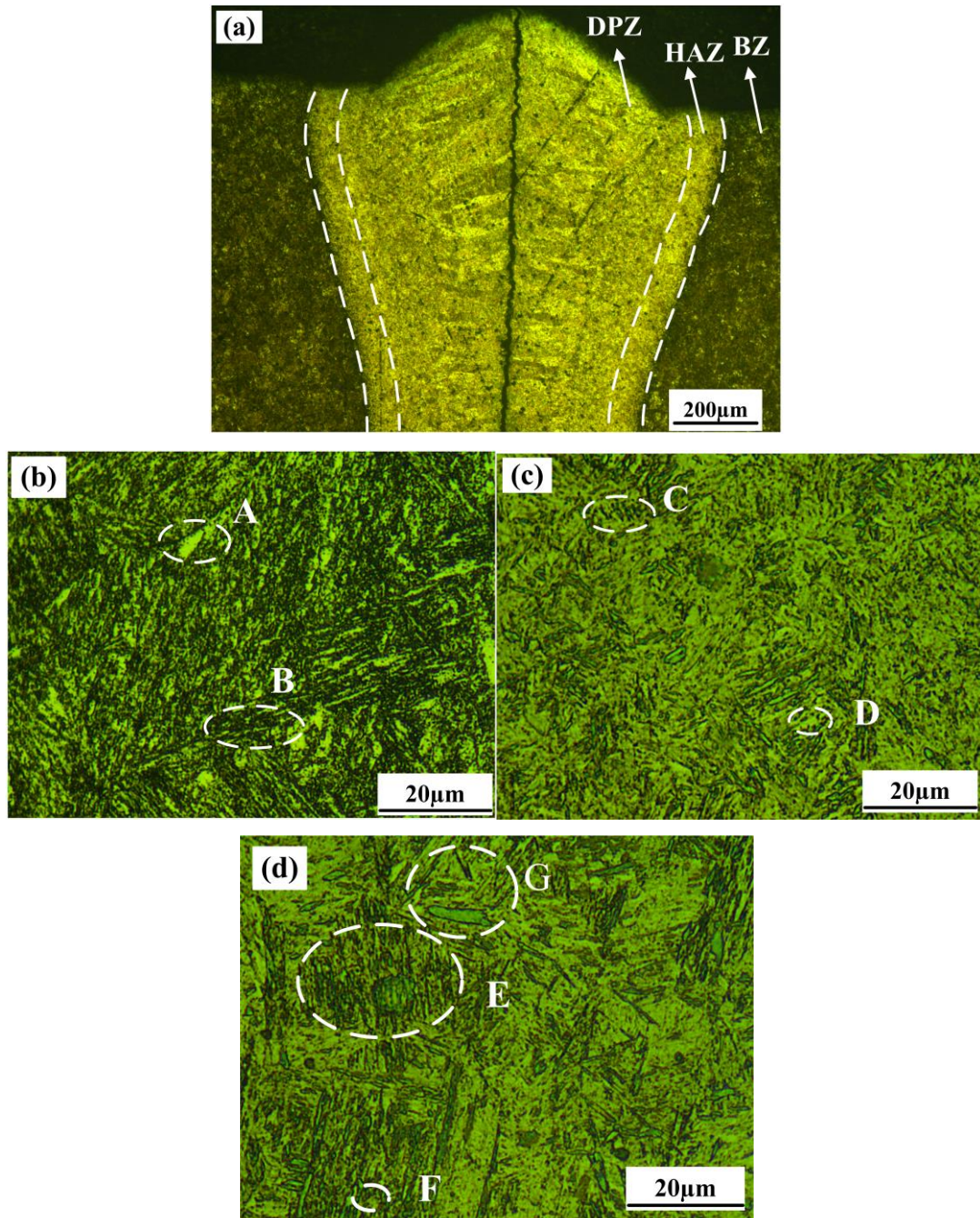


Fig. 5 SEM examination of microstructure in L-3. (a) macroscopic morphology; (b) magnify of the base material (BM); (c) magnify of the heat affected zone (HAZ); (d) magnify of the deep penetration zone (DPZ)

Furthermore, the residual austenite that are mixed with lath martensite also appears in different zones such as region B, D, and F. The austenite is unlikely to transform to martensite completely because final temperature of martensitic transformation (M_f) is lower than room temperature and the cooling rate is fast in LDPP. The similar results were also obtained by others [23, 24].

As shown in **Fig. 6**, the values of average microhardness in DPZ is about twice as much as the BM in L-1, L-2, and L-3 [25, 26], and the value of microharness in

DPZ tend to decrease when HI is from 27 J/mm to 240 J/mm. However, the values of microhardness of L-1 and L-4 are not as high as that of L-3 near the center of deep penetration zone (in region A) in **Fig. 6**. And in region A, it can be seen that the values of microhardness of L-1 and L-4 are very close. The sudden increase of hardness value is due to the appearance of a large amount of martensite in DPZ (in Fig. 5), and it leads to the increase of brittleness in DPZ. The brittleness increases the cracking tendency in DPZ. Thus, the cracking tendency of L-3 is more obvious than that of L-1 and L-4. In fact, there is a central crack in DPZ of L-3 (Fig. 4) indeed.

The appearance of martensite and higher microhardness in DPZ is advantageous to the formation of cracks. This is of great significance for pre-controlled cracks.

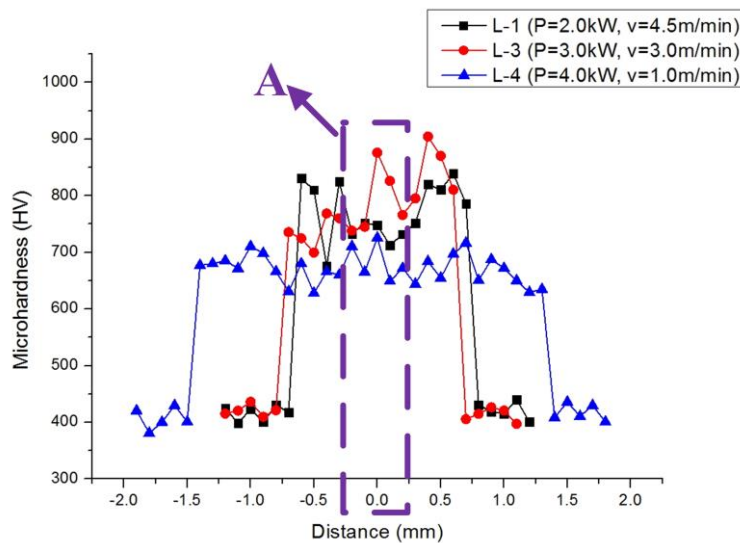


Fig. 6 Distribution of the microhardness.

3.3 Fracture morphology analysis

A thorough examination of the fracture morphology (number L-3) using a SEM is shown in **Fig. 7**. From image (a), it can be seen that various tearings are revealed at the top of DPZ. These tearings is attributed to intergranular fracture caused by a large number of columnar crystals in region B of image (b). Meanwhile, the transgranular mode is also evident in region A. Thus, the fracture mode at the top of DPZ is a mixed fracture, that is the intergranular and transgranular fracture. This is a typical brittle fracture.

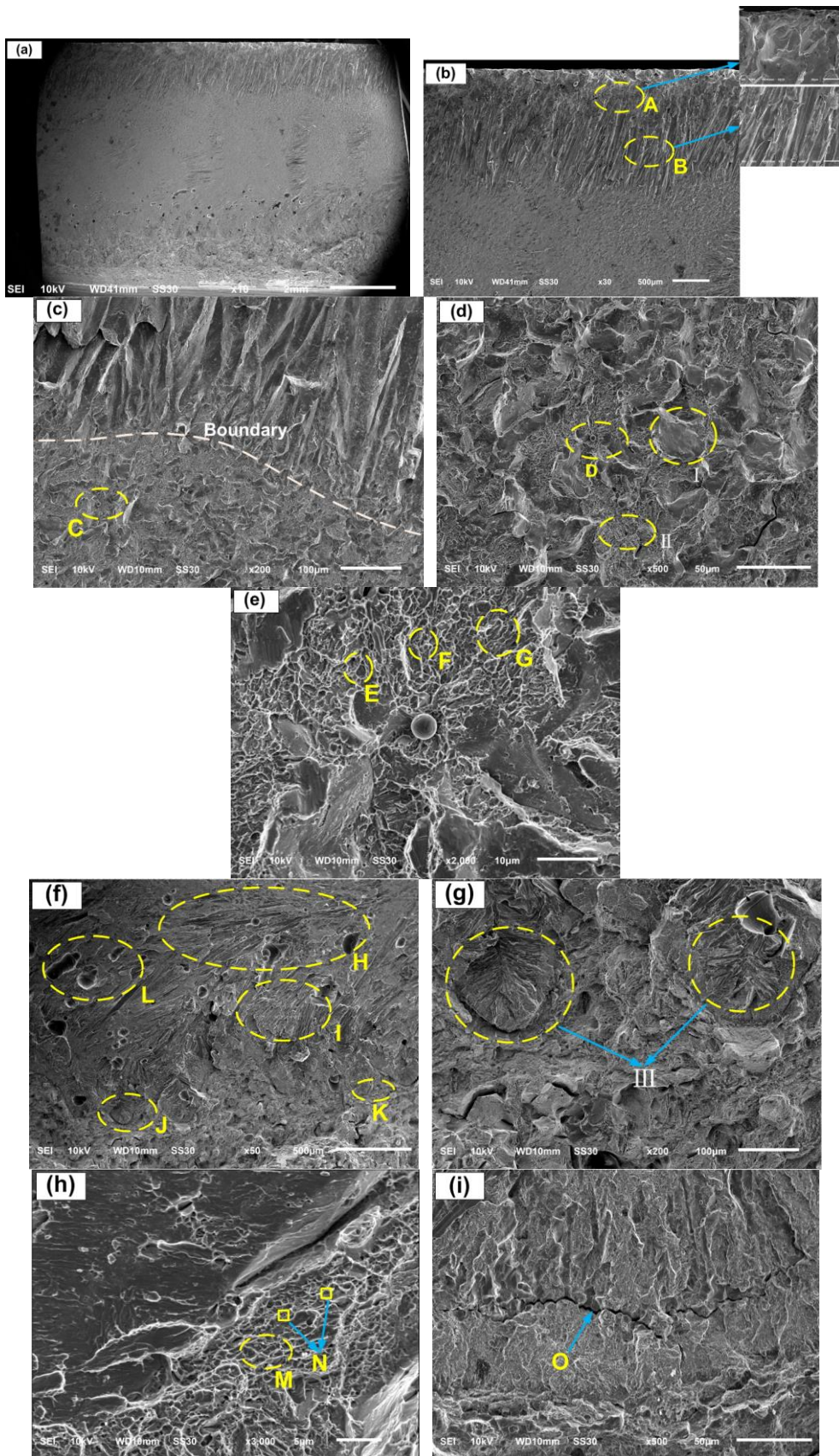


Fig. 7 SEM examination of fracture morphology in L-3. (a) integral morphology; (b) morphology at the top area in DPZ; (c) morphology in the middle area; (d) and (e) are the magnification of region C and D, respectively; (f) and (i) are the morphology in the rear area in DPZ; (g) and (h) are the magnification of region J and K, respectively.

Then, it can be seen that there are more details about the fracture mode in the middle of DPZ from image (h), and image (c) to image (e) in **Fig. 7**. From image (c), it can be observed that there is an obvious boundary between the top and middle of DPZ. Moreover, a definitive understanding of fracture mode in the middle area is obtained in image (d) (the magnification of region C). From image (d), there are some dimples (region II) and the cleavage surface (region I). It should be noted that the transition from brittle fracture to ductile fracture is revealed (because of some dimples). For further observation, image (e) (the magnification of region D) reveals more details about these dimples. From image (e), it can be observed that there exist many dimples in different states such as the equiaxed dimples (region F), oval dimples (region E) and elongated dimples (region G). Furthermore, these dimples are characteristics of smaller in size and shallower in depth. These dimples were also observed by other scholars [25, 27]. The reason is that the strain hardening is appeared in DPZ due to the mechanical properties of 50SiMnVB steel and appearance of martensite [28]. According to the theory of back stress [29], the formation mechanism of dimples can be regarded as stress equilibrium. It caused by the accumulation of the Orowan rings (a kind of dislocation) around the particles or inclusions without the external force, and then Orowan ring moves to the grain boundary to form various micropores under the shear stress. When shear stress increases, micropores tend to form the dimples. In other words, dimples are easier to form around the second phase particles or inclusions. In this study, it should noted that some particles are presented in region N from image (h). This is supported by the the theory of back stress. Thus, the fracture mode in the middle of DPZ is the ductile and brittle fractures.

Lastly, it can be seen that there are more details about the fracture mode in the rear area of DPZ from image (f) and image (i) in **Fig. 7**. From image (f), it can be observed that there reveals a river-like pattern and intergranular fracture corresponding to region H and I, respectively. The river-like pattern is one of a major feature in cleavage fracture and it is characteristics of each branch gathering in one place (a mainstream), a sketch map can be seen from **Fig. 8**. The group of cracks and surface steps are one of the necessary conditions for the straight leading edge crack transfer to the new inclined plane along the whole front end of crack [30]. Furthermore, from image (g) (the magnification of region J) in **Fig. 7**, the herringbone pattern is also revealed in region III. The middle fish ridge line is a specific cleavage surface (crystallographic plane). Similarly, it is also one of the features in cleavage fracture. Moreover, from image (h) (the magnification of region K) in **Fig. 7**, there are some dimples in region M too. It is important to point out that the number of dimples are not as many as image (e) in **Fig. 7**. In other words, the fracture mode is still dominated by brittle fracture. From image (f) and (i) in **Fig. 7**, it can be observed that there reveals more defects (in region L) than other areas and the branching cracks (in

region O), respectively. It should be pointed out that energy in plastic deformation releases at the tip of cracks owing to the stress concentration [17, 31, 32] and it make the cracks prolong. In other words, it is illustrated that the defects are more likely to be formed at the tip of DPZ (in the rear), and they might be the crack sources [33]. This is consistent with image (b) in **Fig. 4** of the section 3.1 in this research. Thus, the fracture mode in the rear of DPZ is the ductile and brittle fractures, however, brittle fracture is dominant.

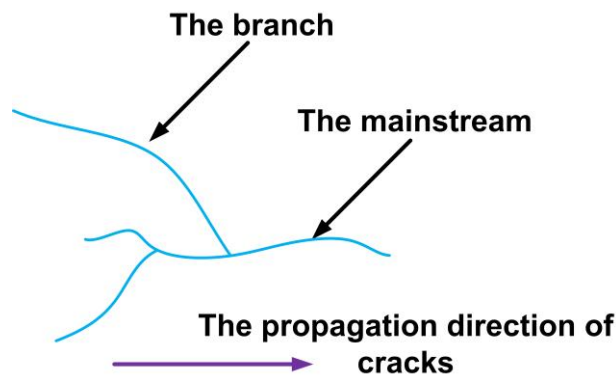


Fig. 8 Sketch map of propagation direction of cracks [30].

An SEM examination of cross-sectional morphology is shown in **Fig. 9**. As can be seen from region A in image (a), the incomplete grains emerge. It is illustrated that the transgranular fracture exists indeed. Moreover, secondary cracks are also observed in region B and C. The results are in coincide with image (b) and (i) in **Fig. 7**.

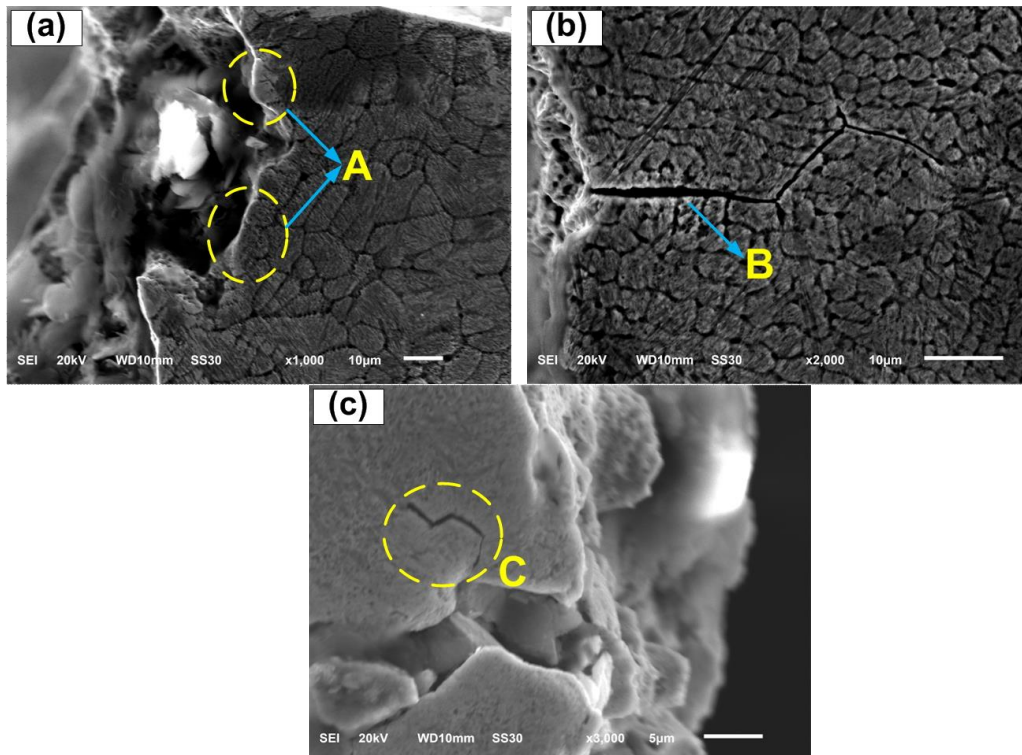


Fig. 9 SEM examination of cross-sectional morphology in L-3. (a) and (b) are both the left side morphology of central crack; (c) the right side morphology of central crack.

In conclusion, the brittle fracture (the intergranular and transgranular fracture) occurred at the top area in DPZ. The mixed-mode of ductile and brittle fracture is

revealed in the middle and rear areas. The diagrammatic sketch is presented in **Fig. 10**. It is important to point out that the existence of martensite has a great influence on the fracture mode.

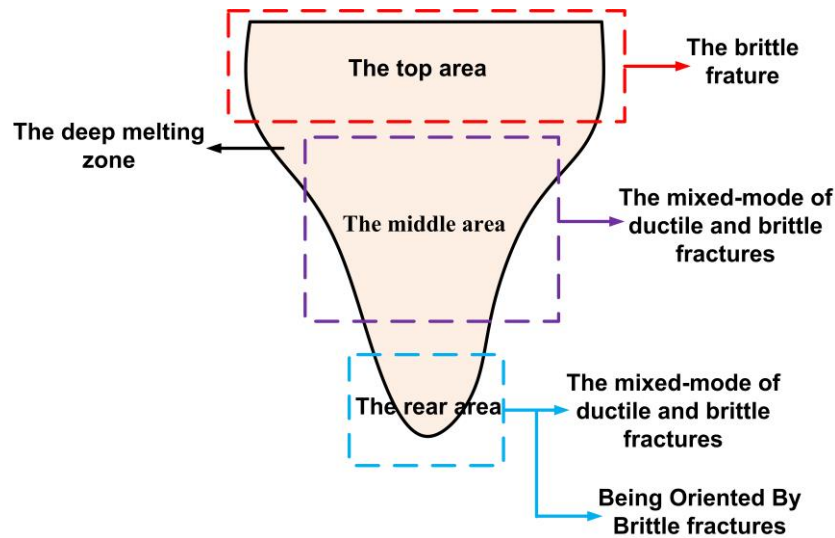


Fig.10 Diagrammatic sketch of the fracture mode in different areas in deep penetration zone.

Furthermore, hot crack is one of the main feature in intergranular fracture. According to the theory of liquid film [34], the cracking of liquid film is caused by the shrinkage stress of solidification (laser deep penetration processing is a typical rapid heating/rapid cooling non-equilibrium process [35]). The stress destroys the bonding force of liquid film between crystals. A schematic diagram of liquid film cracking mechanism is shown in **Fig. 11**.

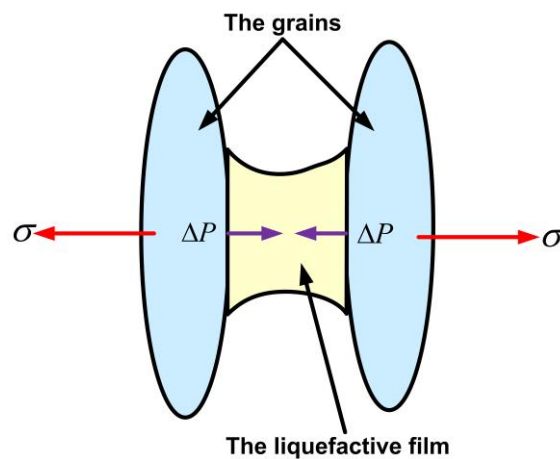


Fig. 11 A schematic diagram of liquid film cracking mechanism [34].

However, the hot cracks are unlikely to penetrate entire DPZ because a severe intergranular fracture mode is only appeared at the top area. It should be noted that cold cracks is the main feature of transgranular fracture (It can be seen in **Fig. 9**). Thus, it is believed that the central crack is a result of propagation of cold crack along the hot cracks. The cold crack will be further discussed in section 3.4.

3.4 Simulation analysis

SYSWELD (numerical simulation software that was developed by France's

Framatome company and ESI company in 1980) is used in this research in order to analyze the cracking mechanism and fracture mode in DPZ. And the results provide a reasonable explanation for the cracking mechanism and fracture mode from the temperature and stress distribution in DPZ.

3.4.1 Checking heat source and modeling

A 3D Gauss heat source is used in this part , and it can be described with the following formula [36,37]:

$$q(r) = q_m \exp\left(-\frac{3r^2}{r_0^2}\right) \quad (2)$$

$$r_0(z) = r_e - (r_e - r_i) \frac{z_e - z}{z_e - z_i} \quad (3)$$

where q is the heat flux density about r from the center of heat source on the plane with a height of z ; q_m is the maximum heat flux density on the plane with a height of z ; r is the distance from any point belonging to an effective heating area for a heat source to the center of heat source; r_0 is the maximum characteristic radius, and it is related to the ordinate z ; r_e and r_i are both the Gauss parameters, and r_i , r_e have the following relations with x and y : $r_{(i,e)}^2 = x^2 + y^2$; r_0 , r_i and r_e vary with the change of x , y and z ; z_e and z_i are both the position parameters of the 3D Gauss heat source and welding specimens. In **Fig. 12**, it can be seen that the macroscopic morphology of DPZ is coincide with the results from numerical simulation. Moreover, it provides a reasonable condition for simulating the distribution of temperature and stress field.

Due to a severe heat exchange in DPZ, the heat conduction equation (a typical nonlinear transient) in simulation can be seen as follows [35]:

$$\rho(T)c(T)\frac{\partial T}{\partial t} = \frac{\partial}{\partial x}\left(k_x(T)\frac{\partial T}{\partial x}\right) + \frac{\partial}{\partial y}\left(k_y(T)\frac{\partial T}{\partial y}\right) + \frac{\partial}{\partial z}\left(k_z(T)\frac{\partial T}{\partial z}\right) + Q_v \quad (4)$$

where $\rho(T)$ and $c(T)$ are the density and specific heat capacity of materials respectively; Q_v is the energy density of the heat source; $k(x)$, $k(y)$ and $k(z)$ are the heat conduction coefficient along the direction of x , y and z , respectively.

The stress and deformation in DPZ obey Von Mises yield criterion (in the elastic range) and flow criterion (exceeds the elastic range) [38], respectively. Von Mises yield criterion and flow criterion can be described with the following formula, respectively:

$$\bar{\sigma} = \sqrt{[(\sigma_1 - \sigma_2)^2 + (\sigma_2 - \sigma_3)^2 + (\sigma_3 - \sigma_1)^2]/2} \leq \sigma_s \quad (5)$$

Where $\bar{\sigma}$ is the equivalent stress; σ_x , σ_y , and σ_z are the positive stresses along the direction of x , y and z , respectively; And σ_s is the yield strength.

$$\{d\varepsilon\}_p = d\lambda \frac{\partial \bar{\sigma}}{\partial \{\sigma\}} \quad (6)$$

where $\bar{\sigma}$ is the quantity function; $\{\sigma\}$ is the vector function; $\{d\varepsilon\}_p$ is the increment of plastic strain; and $d\lambda$ is the plastic multiplier.

About the boundary conditions of simulation, the heat flux at boundary can be seen as follows:

$$q_s = \left. \frac{\partial T}{\partial n} \right|_s = q_s(x, y, z, t) \quad (7)$$

the heat exchange at the boundary is radiative and convective heat transfer are determined by the formula (6) and (7), respectively:

$$-\lambda \left. \frac{\partial T}{\partial n} \right|_s = \varepsilon C_0 (T_s^4 - T_f^4) \quad (8)$$

$$-\lambda \left. \frac{\partial T}{\partial n} \right|_s = \alpha_c (T_s - T_f) \quad (9)$$

where q_s is the heat flux; ε is the optical density; C_0 is the absolute optical density radiation coefficient; T_s is the temperature at the boundary; T_f is the ambient medium temperature; α_c is the convective heat transfer coefficient.

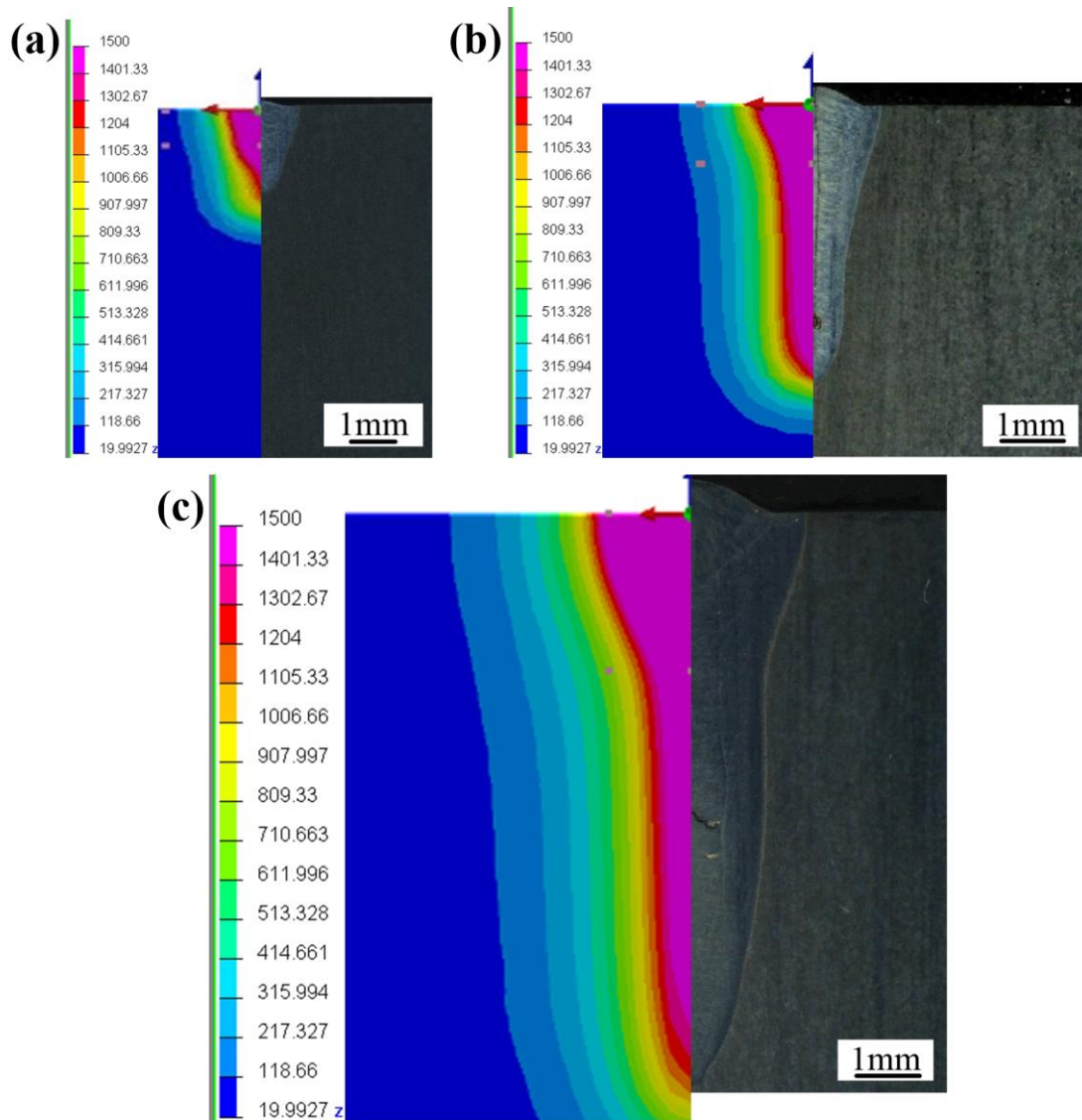


Fig. 12 Comparison in overall size between simulation model and macro morphology in (a) L-1; (b) L-3; (c) L-4. Among them, the left half and the right half of each image (a, b and c) is the temperature field and the macro morphology, respectively.

3.4.2 Distribution of temperature field in DPZ

As can be seen from image (a) in **Fig. 13**, $T_1 \sim T_2$ (about 1400~1500°C) is a range in temperature of solid-liquid coexistence and it is a main sensitive zone of thermal crack [39, 40]. From image (b), slope of Y is the solidification rate in $T_1 \sim T_2$, and it can be seen that the value of slop in L-3 is larger than L-1 and L-4. It should be pointed out that it can create a severe disturbance (a large amplitude) and solute enrichment on the solid-liquid interface in alloys. Some compounds of low melting point will gather at the grain boundaries, and then hot cracks are easy to form [18].

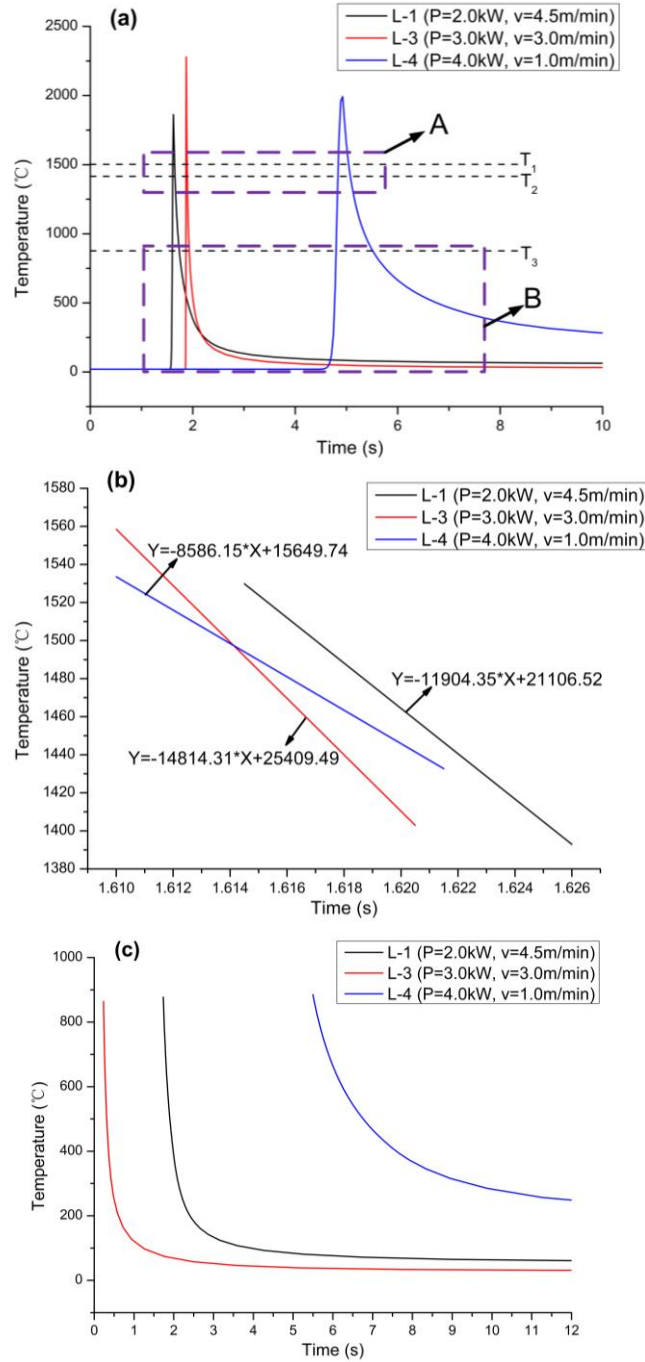


Fig. 13 (a) curve of thermal cycle in L-1, L-3, and L-4; (b) the magnification of region A; (c) the magnification of region B.

Thermal crack sensitivity can be represented by thermal crack sensitivity coefficient (HCS), and it can be seen as follows [37]:

$$HCS = \frac{C(S + P + \frac{Si}{25} + \frac{Ni}{100})}{3Mn + Cr + Mo + V} \times 10^3 \quad (10)$$

where the various element symbols in the formula represent the mass fraction of them. It should be pointed out that the formula (8) is not used in simulation, and it is only a criterion for judging HCS in 50SiMnVB steel. The result shows that the HCS of 50SiMnVB steel is 0.181, it is less than 4. Thus, the thermal crack sensitivity of

50SiMnVB steel is smaller. However, carbon is extremely easy to segregate in the process of solidification and form eutectic (lower melting point) with other elements such as sulfur and phosphorus, etc. [39]. The eutectic products have a feature of low melting point and it will increase the sensitivity of thermal crack.

From image (a) in **Fig. 13**, T_3 (about 850°C) is a starting temperature of quenching [15]. The cold crack has a relationship with the cooling rate after T_3 [41, 42]. As shown in image (c), the value of cooling rate after T_3 in L-3 is also larger than the others. Jackson et al. [43] made it clear that a high magnitude of transient driving force makes the transient energy release rate increase sharply, and cracks extend instantaneously. These results are consistent with the observation from section 3.3.

Similarly, a trend of cold crack can be determined by the carbon equivalent (C_{eq}) [41]:

$$C_{eq}(AWS) = C + \frac{Mn}{6} + \frac{Si}{24} + \frac{Ni}{15} + \frac{Cr}{5} + \frac{Mo}{4} + \left(\frac{Cu}{13} + \frac{P}{2}\right) \quad (11)$$

where the various element symbols in the formula represent the mass fraction of element. It should be pointed out that the formula (9) is not used in simulation. It is only a criterion for judging a tend of cold crack. The result shows that the C_{eq} of 50SiMnVB steel is 0.851. From **Fig. 14**, it reveals that the tend of cold crack of 50SiMnVB steel is higher.

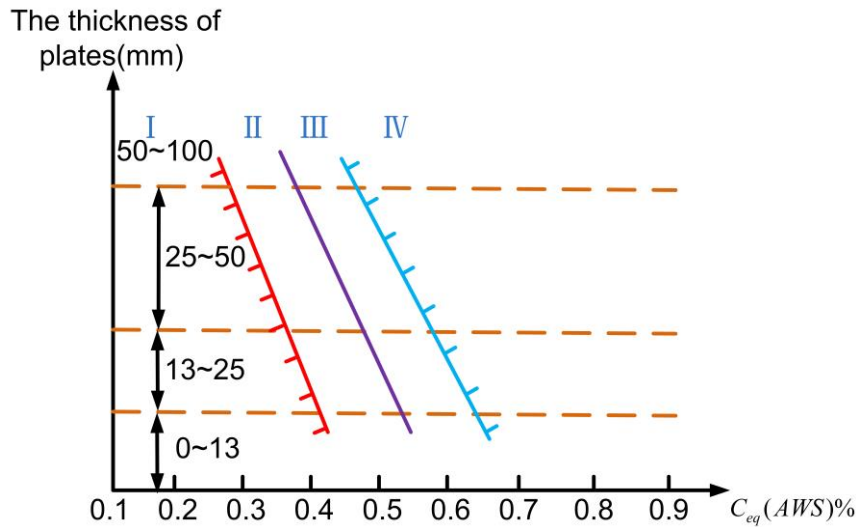


Fig. 14 Grade of welding properties of steels [39].

I : Excellent II: Good III: Qualify IV: Poor

Moreover, as can be seen from **Fig. 15**, the cooling rate at the top area of DPZ is highest, followed by middle area and finally is rear area. Significantly, Chen et al. [44] pointed out that the fracture mode can change from brittle fracture to ductile fracture when the cooling rate decrease. The conclusion obtained in section 3.3 is supported by Chen et al.

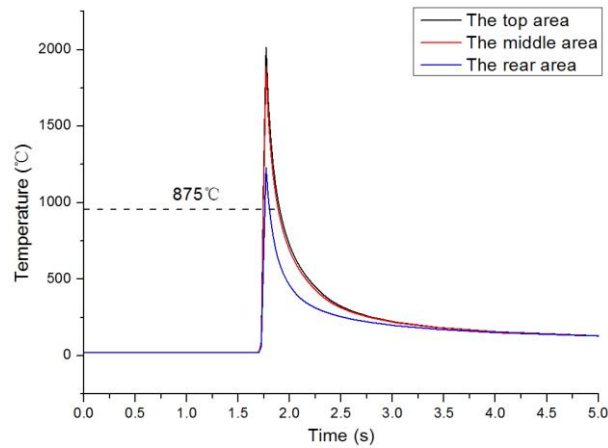


Fig. 15 Curve of thermal cycle in L-3 in different zones.

3.4.3 Distribution of stress field in DPZ

As shown in **Fig. 16** (b), there is a magnitude of tensile stress in the entire DPZ in L-3. However, a magnitude of tensile stress is only on the edge of DPZ in L-1 and L-4. It is illustrated that the propagation of central crack is easier to be formed in L-3 than those of L-1 and L-4 because the stress intensity factor increases [17]. Furthermore, in **Fig. 17**, it can be seen that there is a higher tensile stress (about 140MPa) in the center of DPZ when the solidification process is finished. The above results indicate that the cold cracks penetrate DPZ and the central cracks due to the residual tensile stress [39,45].

In conclusion, the main reason of central cracks appearing in DPZ including (a) The appearance of martensite increases hardness and a tendency to crack increases; (b) The trend of cold crack of 50SiMnVB steel is higher because of its poor weldability in laser processing; and (c) A high magnitude of tensile stress and rapid cooling rate causes the DPZ cracking.

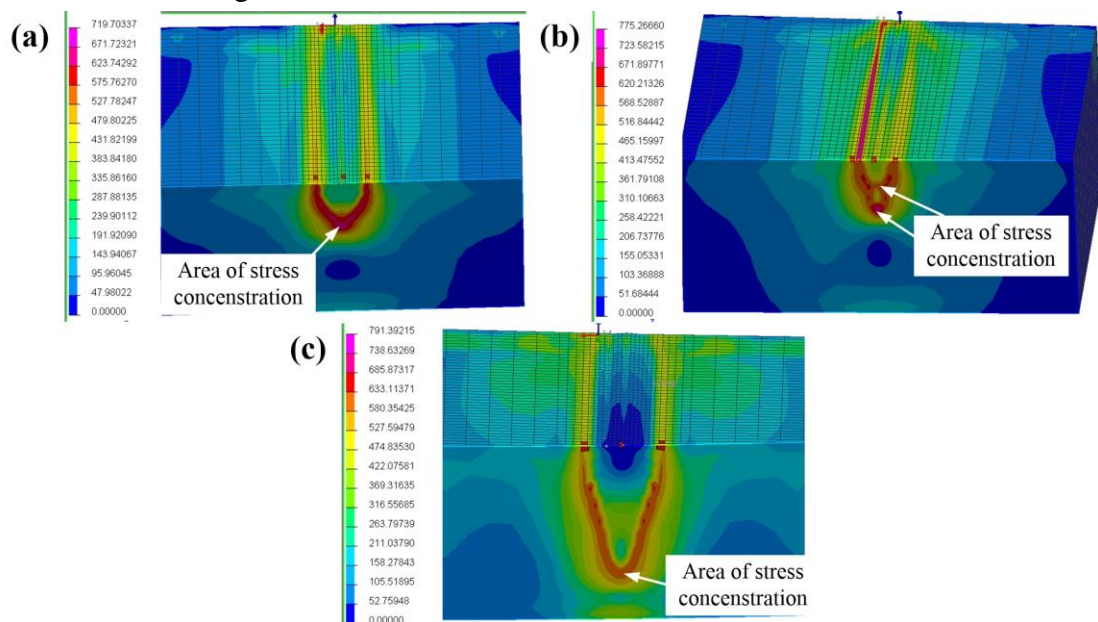


Fig. 16 Distribution of the stress field in (a) L-1; (b) L-3; (c) L-4.

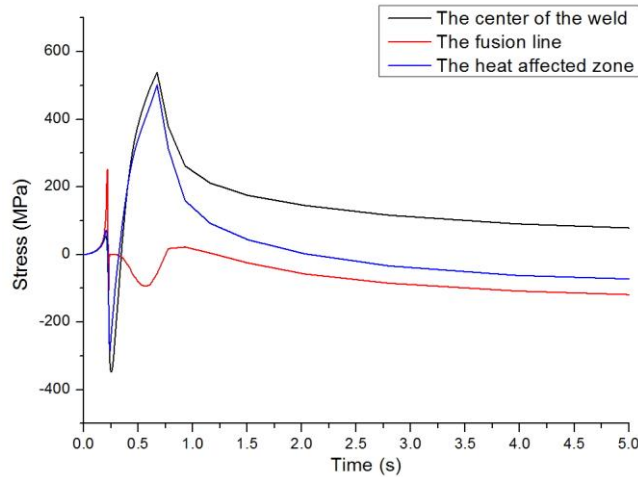


Fig. 17 Curve of stress cycle in L-3.

4. Conclusion

In this study, the following specific conclusions can be drawn:

1. The depth, width, and ratio of depth to width basically increase when HI increase. However, there is little difference in the melting width when HI are 27 J/mm, 51 J/mm, and 60 J/mm. Moreover, there are central cracks in DPZ when HI is moderate (51 J/mm and 60 J/mm), and the crack attaching to 60 J/mm is deeper than that of 51 J/mm.

2. There are massive lath martensite and residual austenite in BM, HAZ and DPZ. However, the martensite existing in HAZ is smaller than the others. Furthermore, the values of average microhardness in DPZ is about twice as much as the BM in L-1, L-2, and L-3, and the value of microhardness in DPZ tend to decrease when HI is from 27 J/mm to 240 J/mm

3. The brittle fracture (intergranular and transgranular fractures) occurs at the top area in DPZ. However, the mixed-mode of ductile and brittle fractures is revealed in the middle and rear areas. In the rear areas, brittle fracture is dominant.

4. There is a magnitude of tensile stress in the entire DPZ in L-3 (60 J/mm). However, a magnitude of tensile stress is only on the edge of DPZ in L-1 (27 J/mm) and L-4 (240 J/mm). Moreover, the solidification rate Y and the cooling rate are significant to the formation of hot crack and cold crack, respectively. Both of them are highest in L-3 (60 J/mm) than the others. The fracture mode changes from brittle fracture to ductile fracture when the cooling rate decrease.

5. LDPP can produce the satisfactory central cracks in the DPZ, and it is of great significance to controlled fragmentation technology.

Declarations

Competing interests statement: The authors declared that they have no conflicts of interest to this work. We declare that we do not have any commercial or associative interest that represents a conflict of interest in connection with the work submitted.

Availability of data and materials statement: All data included in this study are available upon request by contacting with the corresponding author.

Funding: The Equipment pre-research field Foundation of China (Grant No. 61409230315).

Authors' contributions: Firstly, Prof. Yan Shi designed the experimental method and contributed to the general idea of the article. Then, Dr. Dongwei Liu analyzed the experimental data and results combing the relevant literature and wrote the paper. At last, Prof. Jia Liu revised and polished the words in the paper.

Acknowledgement: The authors are grateful for the financial aids from the Equipment pre-research field Foundation of China (Grant No. 61409230315). Ultimately, this research is supported by Changchun University of Science and Technology.

Reference

- [1] P. Liu, Y. Yin, L. Chang, Y. Xue, Establishing of Johnson-Cook constitutive equation for normalized steel 50SiMnVB, *Ordnance Material Science & Engineering*. 32 (2009) 45-49.
- [2] X.Y. Wang, S.S. Wang, F. Ma, Experimental study on the expansion of metal cylinders by detonation, *Int. J. Impact. Eng.* 114 (2018) 147-152.
- [3] S.H. Yang, Z.Q. Zhang, S.Q. Kou, Study of key technology of fracture splitting of engine connecting rod, *Chinese Internal Combustion Engine Engineering*. 27 (2006) 80-84.
- [4] D. Villano, *Innovative Technologies for Controlled Fragmentation Warheads*, *J. Appl. Mech.* 80 (2013) 1704.
- [5] J.C. Beetle, M. Schwartz, *Survey and Assessment of Fragmentation Materials/Concepts*, 1976.
- [6] D. Zhang, S.J. Harris, D.G. McCartney, The effect of laser transformation notching on the controlled fracture of a high carbon (C70S6) steel, *Mater. Sci. Eng. A*. 489 (2008) 273-284.
- [7] J.C. Ion, *Book Review: Laser Processing of Engineering Materials*.
- [8] C.H. Tsai, C.J. Chen, Application of iterative path revision technique for laser cutting with controlled fracture, *Opt. Lasers. Eng.* 41 (2004) 189-204.
- [9] C. Zhang, W. Guan, Z.G. Yang, Z.F. Liu, Optimization of technology parameters for fracture splitting grooves of connecting rods fabricated by pulse fiber laser, *Laser Technology*. 42 (2018) 422-426.
- [10] L. Zheng, S. Kou, S. Yang, L. Li, F. Li, A study of process parameters during

- pulsed Nd:YAG laser notching of C70S6 fracture splitting connecting rods, *Opt. Lasers. Eng.* 42 (2010) 985-993.
- [11] R. Riva, M.S.F. Lima, N.A.S. Rodrigues, J.C.M. Cardoso, Using an Ytterbium fiber laser to fracture splitting of compacted graphite iron bearing caps, *Proceedings of the Fourth International WLT-Conference on Lasers in Manufacturing*, 2007.
- [12] M. Matsumoto, *Scribing with laser*, US, 2002.
- [13] Z. Gu, S. Yang, S. Ku, Y. Zhao, X. Dai, Fracture splitting technology of automobile engine connecting rod, *Int. J. Adv. Manuf. Technol.* 25 (2005) 883-887.
- [14] F.T. Liu, S.Q. Yuan, J. Chen, C.H. Zhou, Comparative study on the shell power after high-energy-beam controlled fragmentation, *Ordnance Material Science & Engineering*. (2008) 67-70.
- [15] Heat treatment Society of Chinese Mechanical Engineering Society, *Heat treatment manual*, Machinery Industry Press, Beijing, 2008.
- [16] M. Pakniat, F.M. Ghaini, M.J. Torkamany, Hot cracking in laser welding of Hastelloy X with pulsed Nd:YAG and continuous wave fiber lasers, *Mater. Des.* 106 (2016) 177-183.
- [17] R. Gadallaha, N. Osawaa, S. Tanakac, S. Tsutsumi, Critical investigation on the influence of welding heat input and welding residual stress on stress intensity factor and fatigue crack propagation, *Eng. Fail. Anal.* 2018.
- [18] W. Kurz, D.J. Fisher, *Fundamentals of Solidification*, CRC Press, 4th edition, 1998.
- [19] Y.L. Hu, X. Lin, K. Song, X.Y. Jiang, H.O. Yang, W.D. Huan, Effect of heat input on cracking in laser solid formed DZ4125 superalloy, *Opt. Lasers. Eng.* 86 (2016) 1-7.
- [20] J.P. Hirth, *Theory of Dislocation*, John Wiley & Sons Inc, New York, 1982.
- [21] C. Zhu, X. Tang, Y. He, F. Lu, H. Cui, Effect of preheating on the defects and microstructure in NG-GMA welding of 5083 Al-alloy, *J. Mater. Process. Technol.* 251 (2017).
- [22] Z.Y. Xu, *Martensitic transformation and martensite*, Science Press, Beijing, 1999.
- [23] J.P. Oliveira, F.M.B. Fernandes, R.M. Miranda, N. Schell, J.L. Ocañad, Effect of laser welding parameters on the austenite and martensite phase fractions of NiTi, *Mater. Charact.* 119 (2016) 148-151.
- [24] P.H.O.M. Alves, M.S.F. Lima, D. Raabe, H.R.Z. Sandim, Laser beam welding of dual-phase DP1000 steel, *J. Mater. Process. Technol.* 252 (2018).
- [25] X.N. Wang, Q. Sun, Z. Zheng, H.S. Di, Microstructure and fracture behavior of laser welded joints of DP steels with different heat inputs, *Mater. Sci. Eng. A.* 699 (2017) 18-25.
- [26] L. Shao, S. Wu, S. Zhao, J. Ketkaew, H. Zhao, F. Ye, J. Schroers, Evolution of microstructure and microhardness of the weld simulated heat-affected zone of Ti-22Al-25Nb (at.%) alloy with continuous cooling rate, *J. Alloys Compd.* 744 (2018).
- [27] W.J. Hui, C.W. Shao, Y.J. Zhang, S.L. Chen, H. Dong, Influence of Vanadium on Fracture Splitting Property of Medium Carbon Steel, *Journal of Iron and Steel Research*, 23 (2016) 475-483.
- [28] F. Šebek, P. Kubík, J. Hůlk, J. Petruška, Strain hardening exponent role in phenomenological ductile fracture criteria, *Eur. J. Mech. A Solids.* 57 (2016) 149-164.
- [29] M.T. Ma, P.Z. Duan, T.Y. You, *Bauschinger effect in metal alloys and its application in industrial production*, Machinery Industry Press, Beijing, 1994.
- [30] Derek Hell. *Fractography Observing, Measuring and Interpreting Fracture Surface Topography*. X. G. Li, C. F. Dong, etc. Translator. Science Press, 2009: P68-120

- [31] N. Saini, C. Pandey, M.M. Mahapatra, R.S. Mulik, On study of effect of varying tempering temperature and notch geometry on fracture surface morphology of P911 (9Cr-1Mo-1W-VNb) steel, *Eng. Fail. Anal.* 85 (2018) 104-115.
- [32] Y. Zhao, M. Liang, Z. Zhang, M. Jiang, S. Liu, Fracture toughness and fracture behavior of CLAM steel in the temperature range of 450°C- 550°C, *J. Nucl. Mater.* 501 (2018) 200-207.
- [33] Y. Zhai, B. Huang, Z. Zhang, X. Mao, Z. Zhao, Effect of preheating on welding cold crack sensitivity of China low activation martensitic steel, *Fusion Eng. & Des.* 133 (2018) 32-38.
- [34] J.C. Borland, Fundamentals of solidification cracking in welds, part 2. *Welding and Metal Fabrication*, 3 (1979) 99-107.
- [35] M.L. Zhang, H.Q. Sun, W.J. Liu, et al. Boundary liquation and interface cracking characterization in laser deposition of Inconel 738 on directionally solidified Ni-based superalloy, *Scr. Mater.* 53 (2005) 159-164.
- [36] H.S. Carslaw, *Conduction of Heat in Solids*, Oxford University Press, Oxford, 1986.
- [37] C.S. Wu, *Welding Thermal Processes and Weld Pool Behaviors*, CRC Press, 2008.
- [38] Y.Q. Ni, G.W. Meng, *Mechanics of materials*, Machinery Industry Press, Beijing, 2005.
- [39] Y.J. Li, J. Wang, *Analysis and Countermeasures of welding defects*, Chemical Industry Press, Beijing, 2013. P183.
- [40] Crack classification - thermal crack. <https://wenku.baidu.com/view/b10189b3910ef12d2af9e7d4.html>, 2014 (accessed 23 May 2014).
- [41] Y.J. Li, *Welding metallurgy - Weldability of materials*, Machinery Industry Press, Beijing, 2013.
- [42] Z.X. Zhu, K.F. Yao, *Engineering materials*, Tsinghua University Press, Beijing, 2014
- [43] R.W. Jackson, M.R. Begley, Critical cooling rates to avoid transient-driven cracking in thermal barrier coating (TBC) systems, *Int. J. Solids Struct.* 51 (2014) 1364-1374.
- [44] C.Y. Chen, W.S. Hsu, S.F. Chen, Role of Sc on the Glass Forming Ability and Mechanical Properties of Al-Y-Ni-Sc Bulk Metallic, *Mater. Sci. Eng. A.* 725 (2018) 119-126.
- [45] J. Hensel, T. Nitschke-Pagel, D.T. Ngoula, H.T. Beier, D.D. Tchuindjang, U. Zerbst, Welding residual stresses as needed for the prediction of fatigue crack propagation and fatigue strength, *Eng. Fract. Mech.* 2017.

Figures

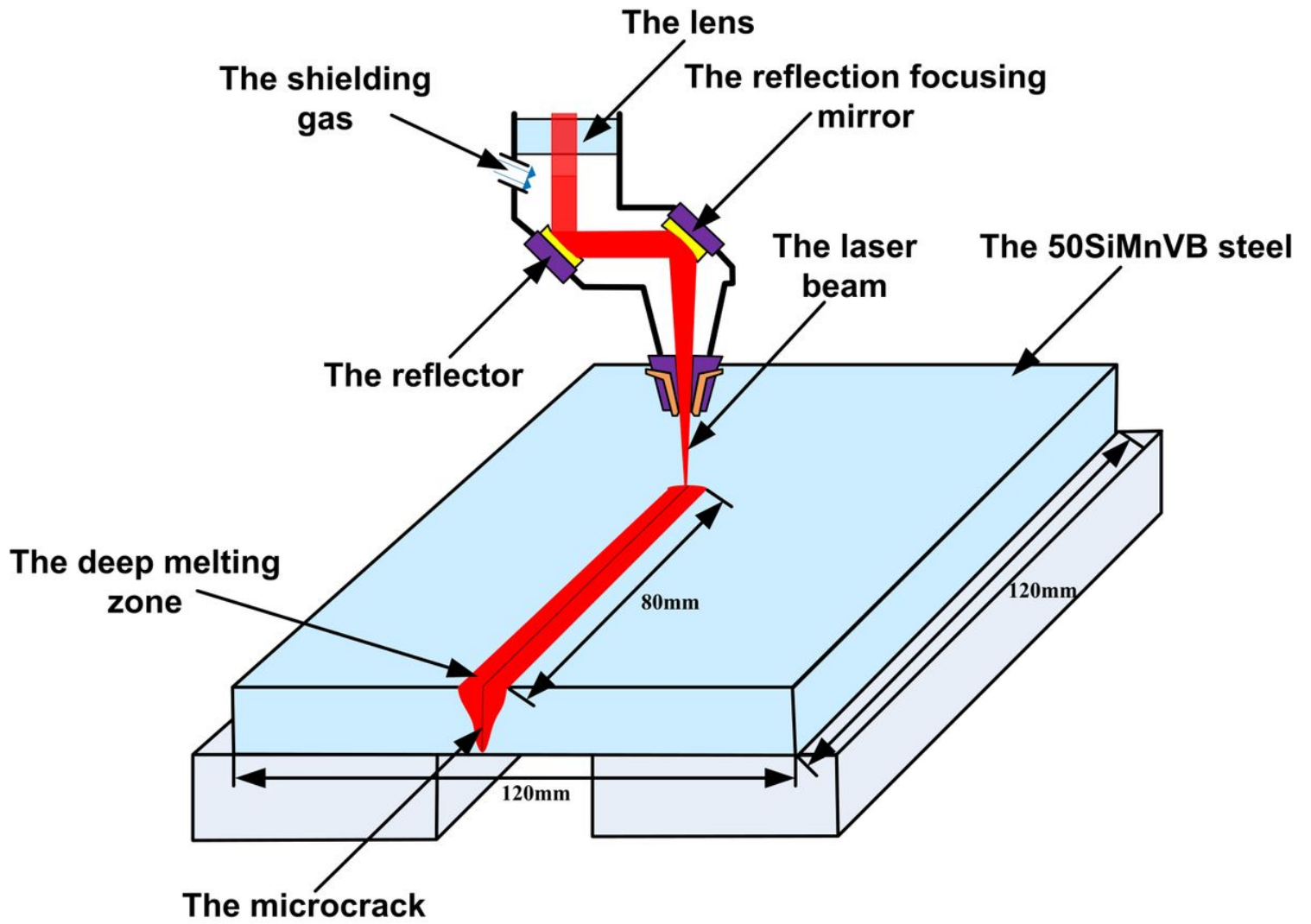


Figure 1

Schematic representation of laser deep penetration processing.

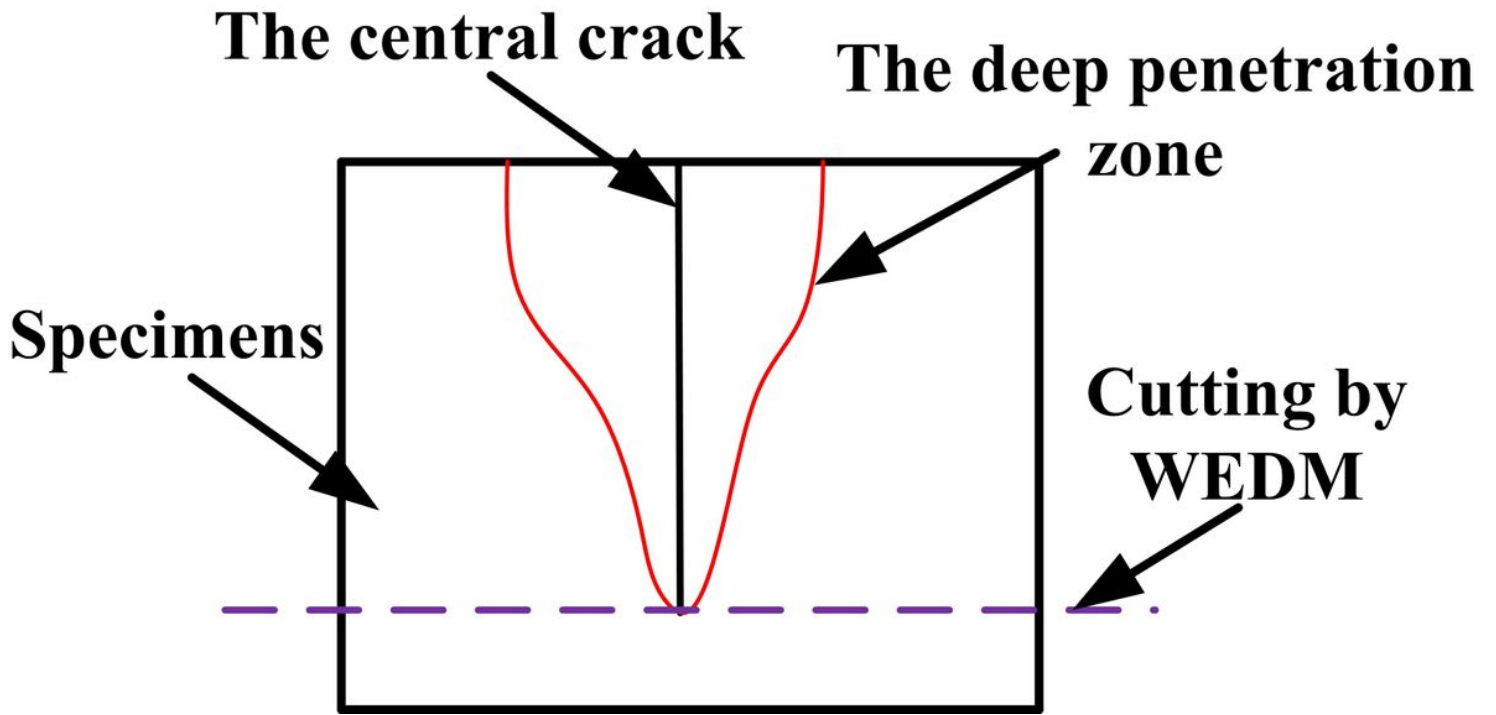


Figure 2

A schematic of sampling fracture morphology.

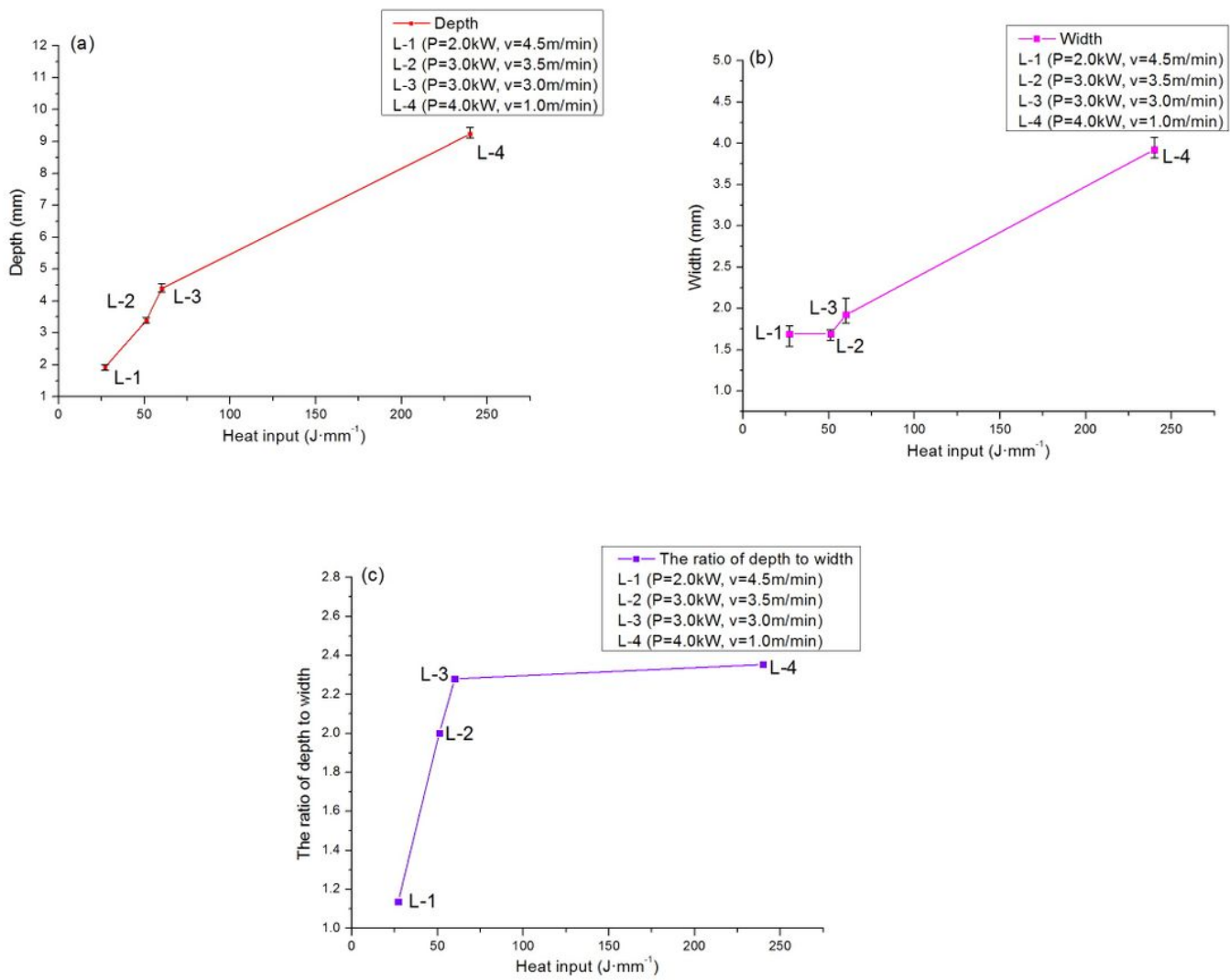


Figure 3

Relationship among the depth, width, the ratio of depth to width and heat input. (a) relationship between the depth and heat input; (b) relationship between the width and heat input; (c) relationship between the ratio of depth to width and heat input.

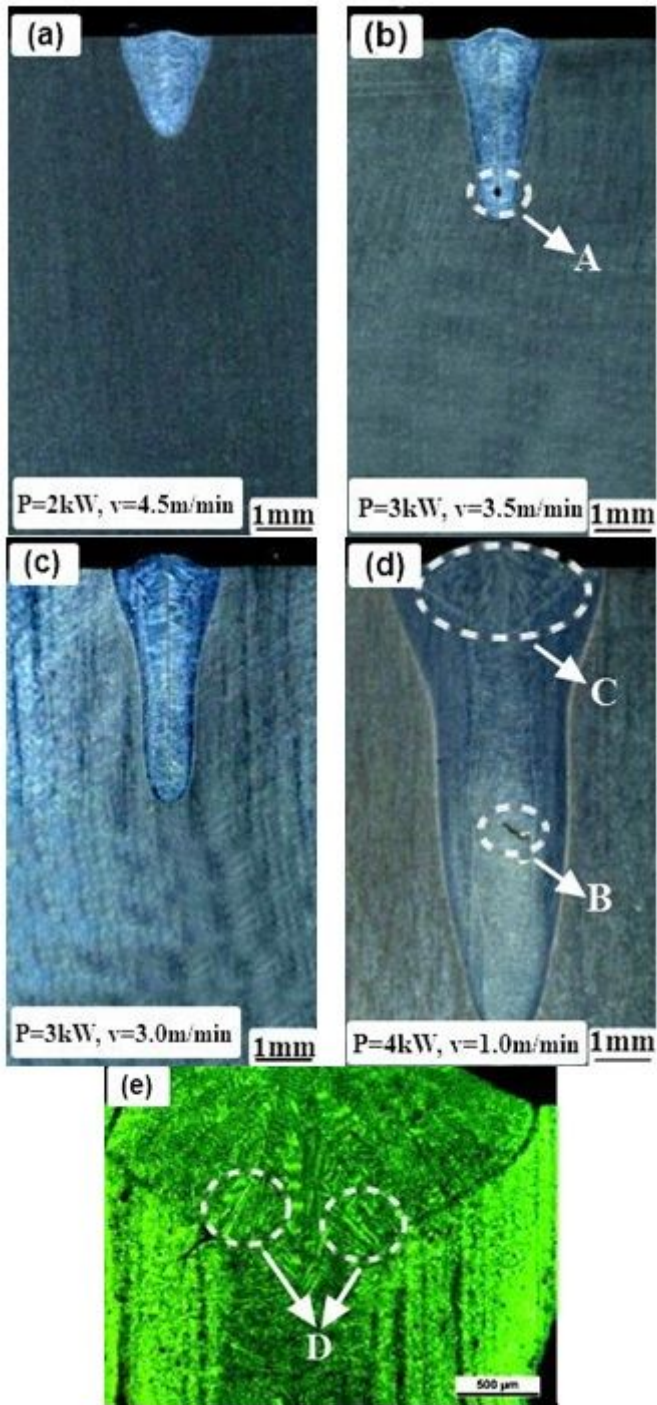


Figure 4

OM examination of (a) L-1; (b) L-2; (c) L-3; (d) L-4; (e) magnify of region C.

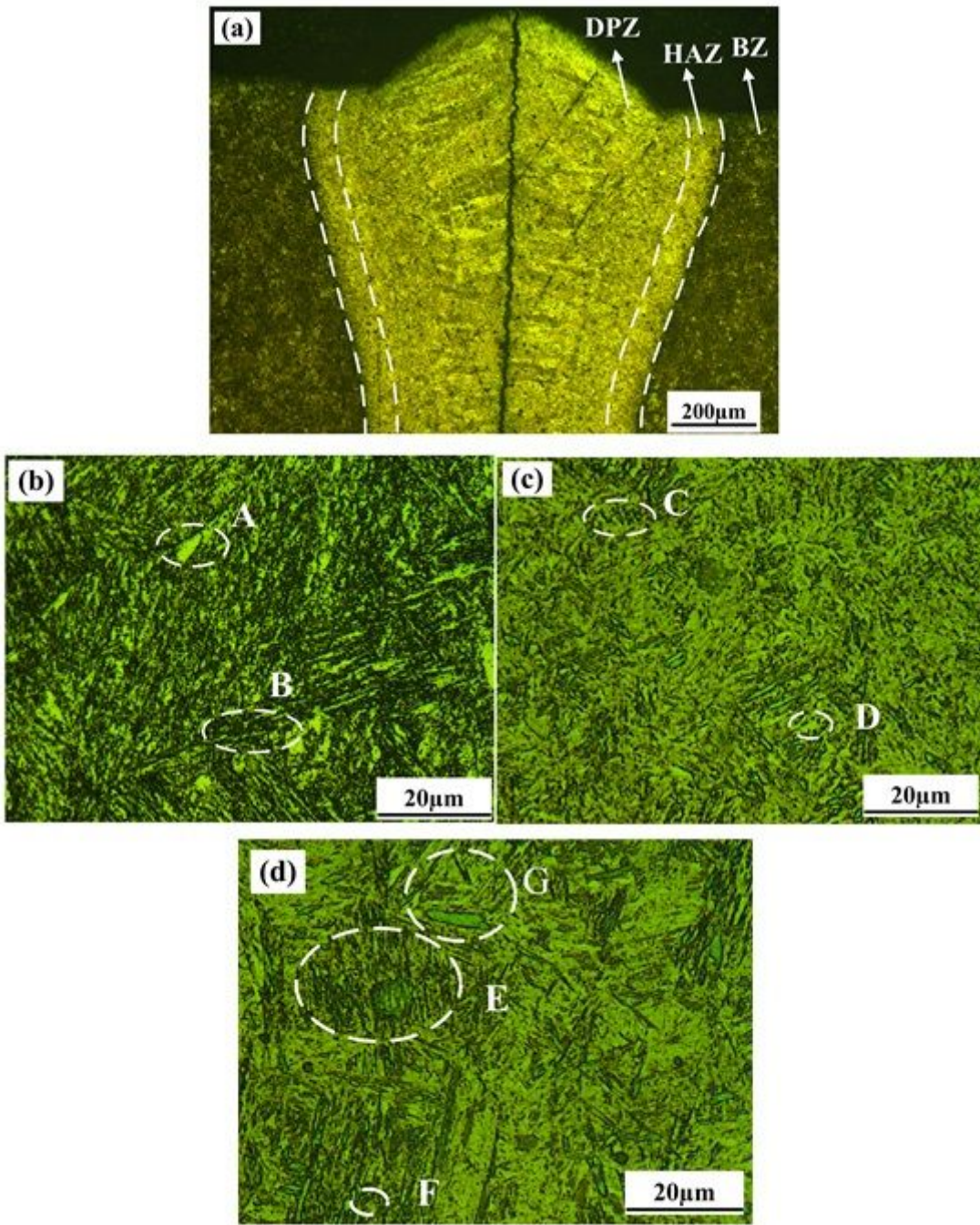


Figure 5

SEM examination of microstructure in L-3. (a) macroscopic morphology; (b) magnify of the base material (BM); (c) magnify of the heat affected zone (HAZ); (d) magnify of the deep penetration zone (DPZ)

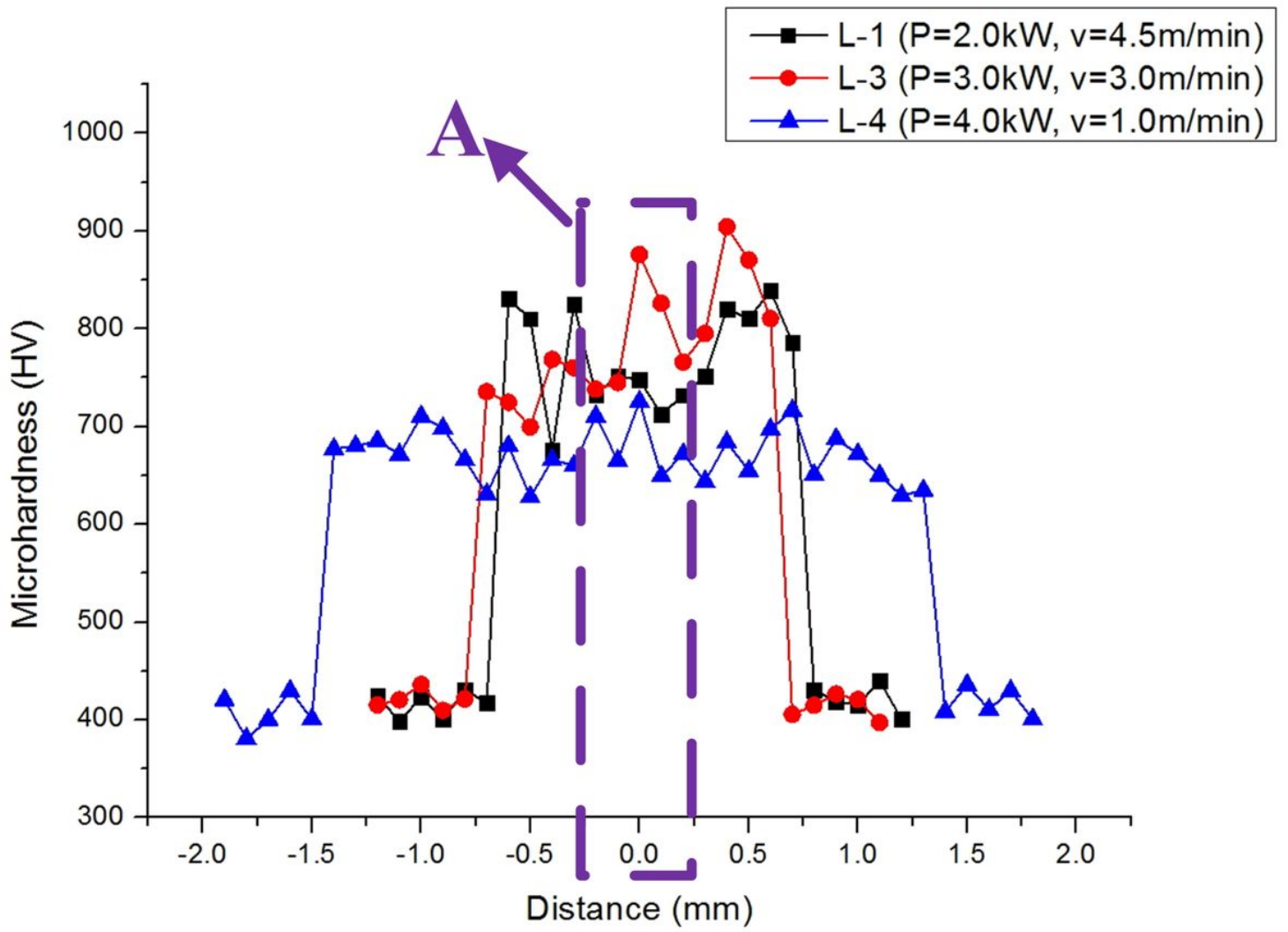


Figure 6

Distribution of the microhardness.

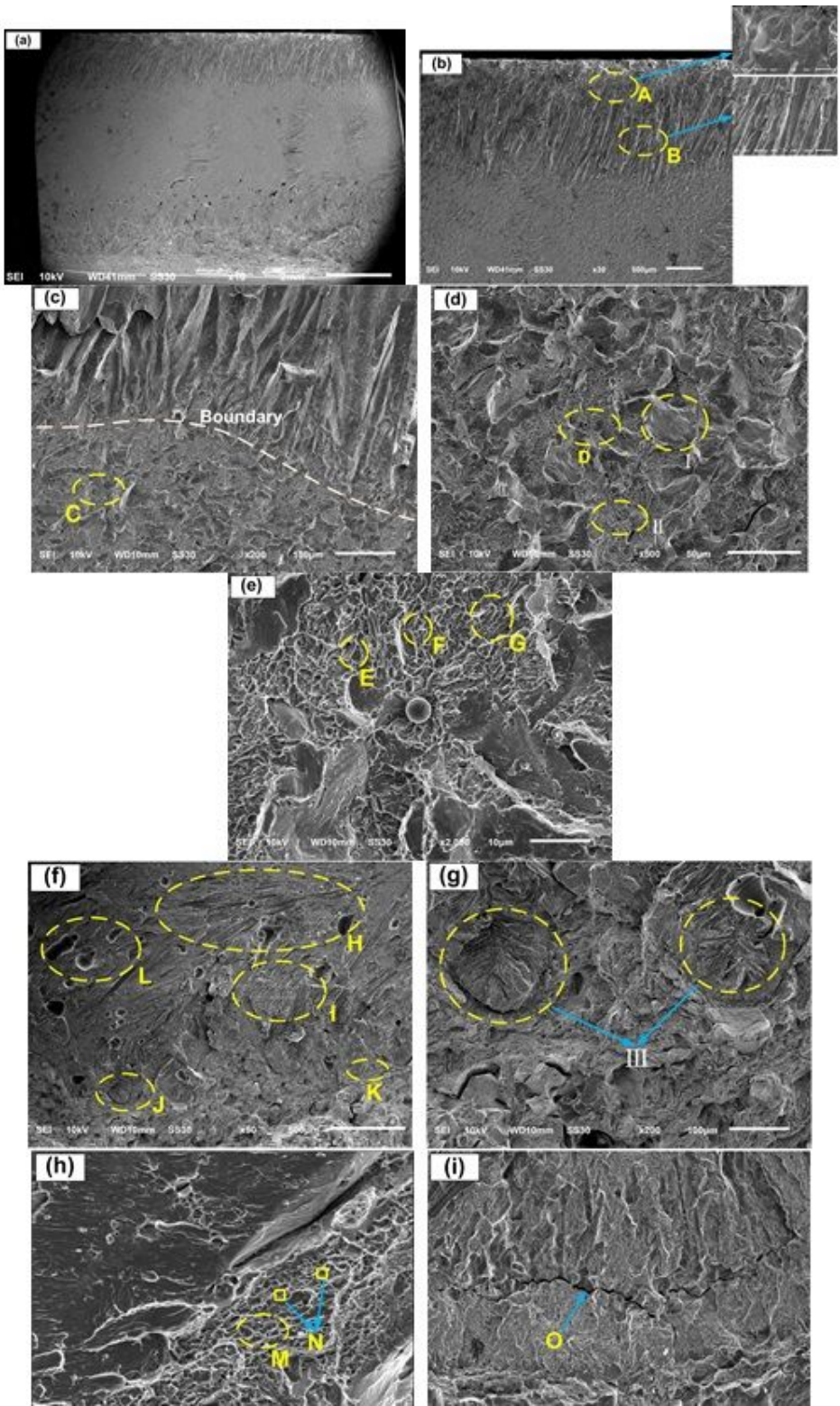


Figure 7

SEM examination of fracture morphology in L-3. (a) integral morphology; (b) morphology at the top area in DPZ; (c) morphology in the middle area; (d) and (e) are the magnification of region C and D, respectively; (f) and (i) are the morphology in the rear area in DPZ; (g) and (h) are the magnification of region J and K, respectively.

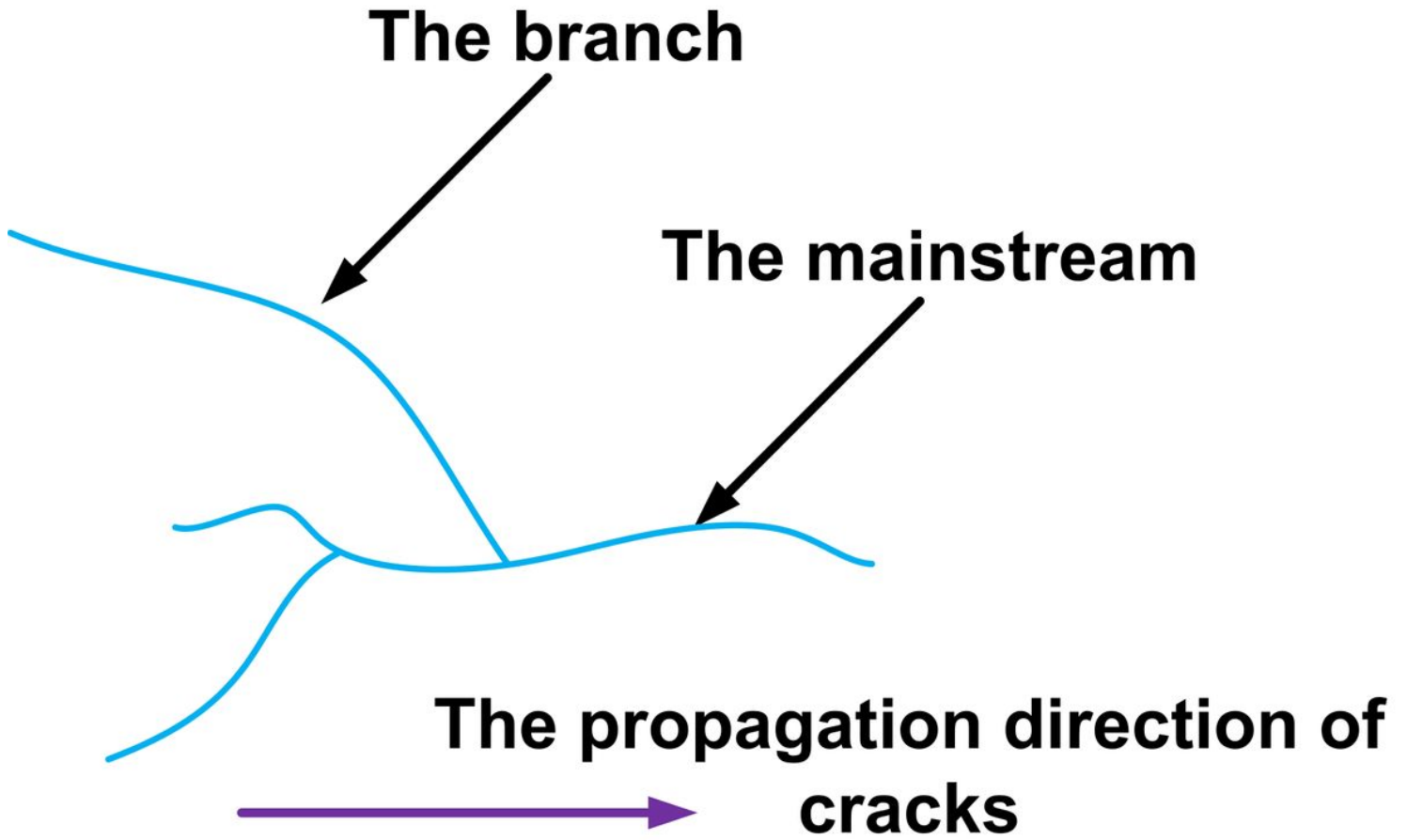


Figure 8

Sketch map of propagation direction of cracks [30].

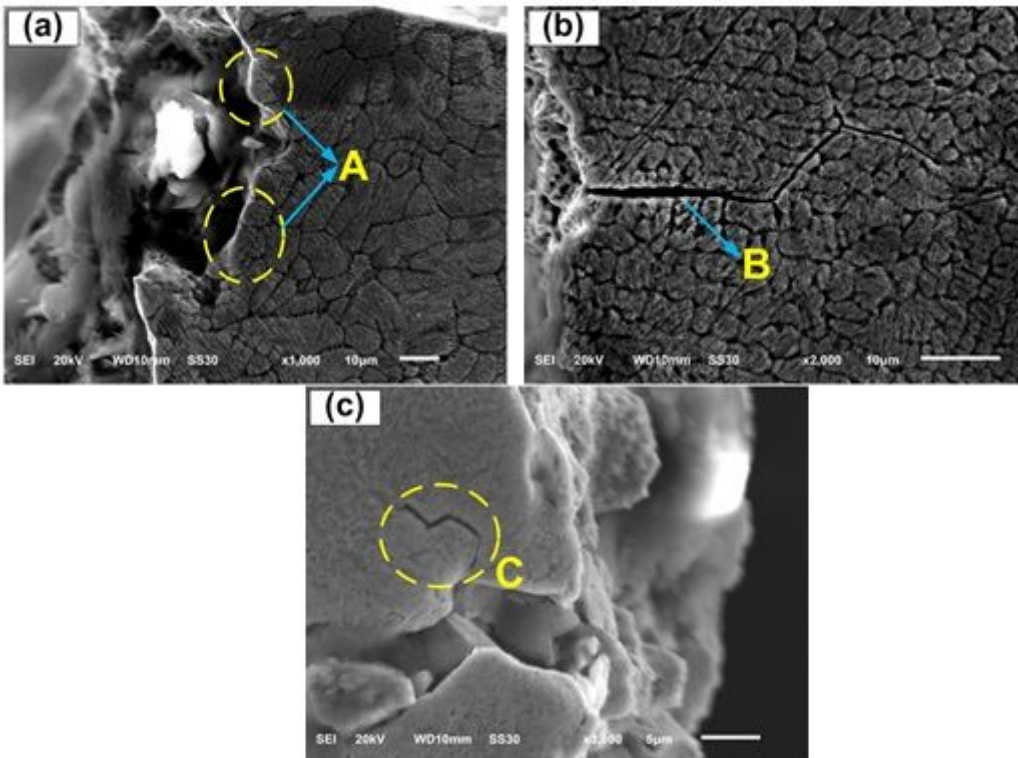


Figure 9

SEM examination of cross-sectional morphology in L-3. (a) and (b) are both the left side morphology of central crack; (c) the right side morphology of central crack.

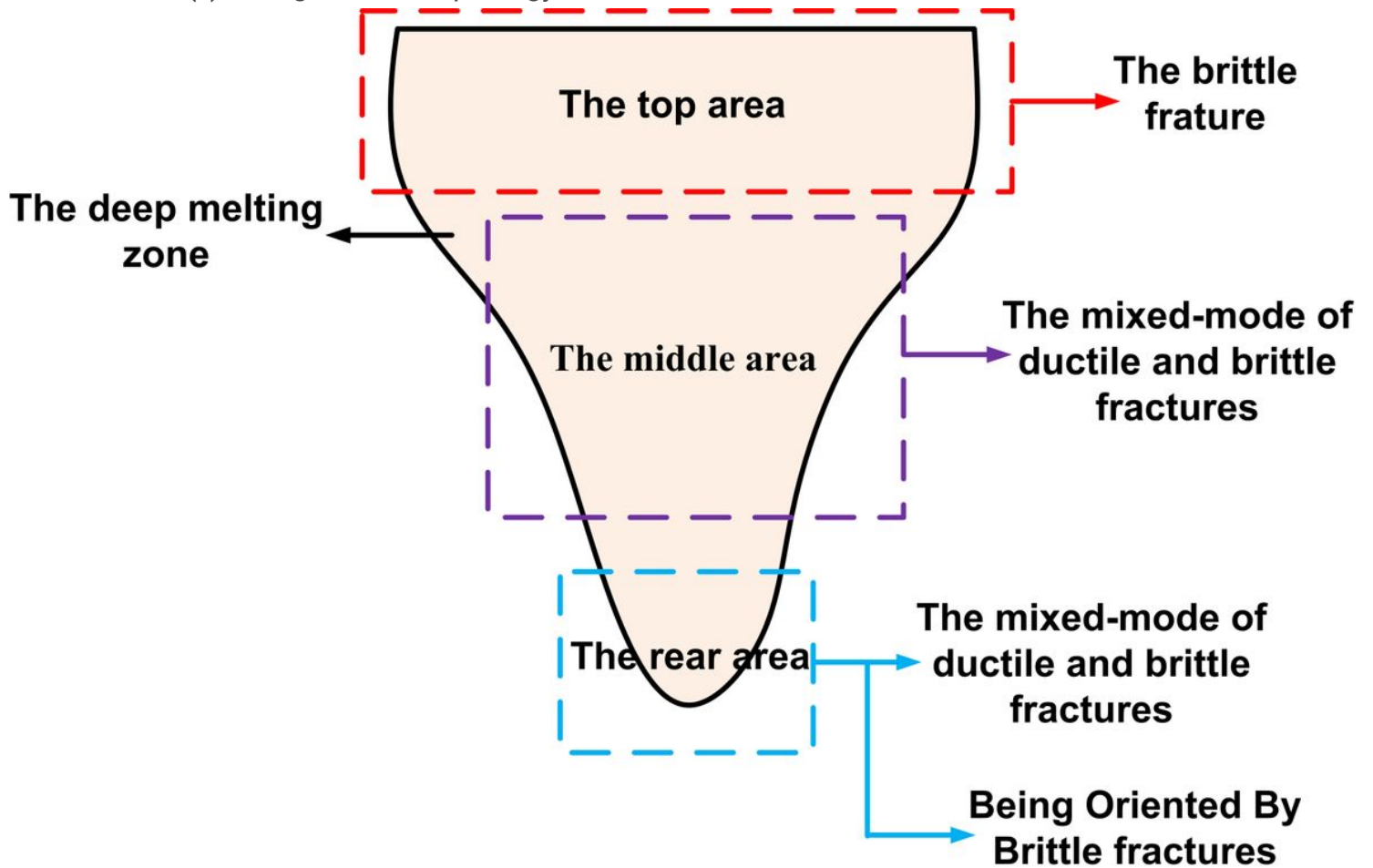


Figure 10

Diagrammatic sketch of the fracture mode in different areas in deep penetration zone.

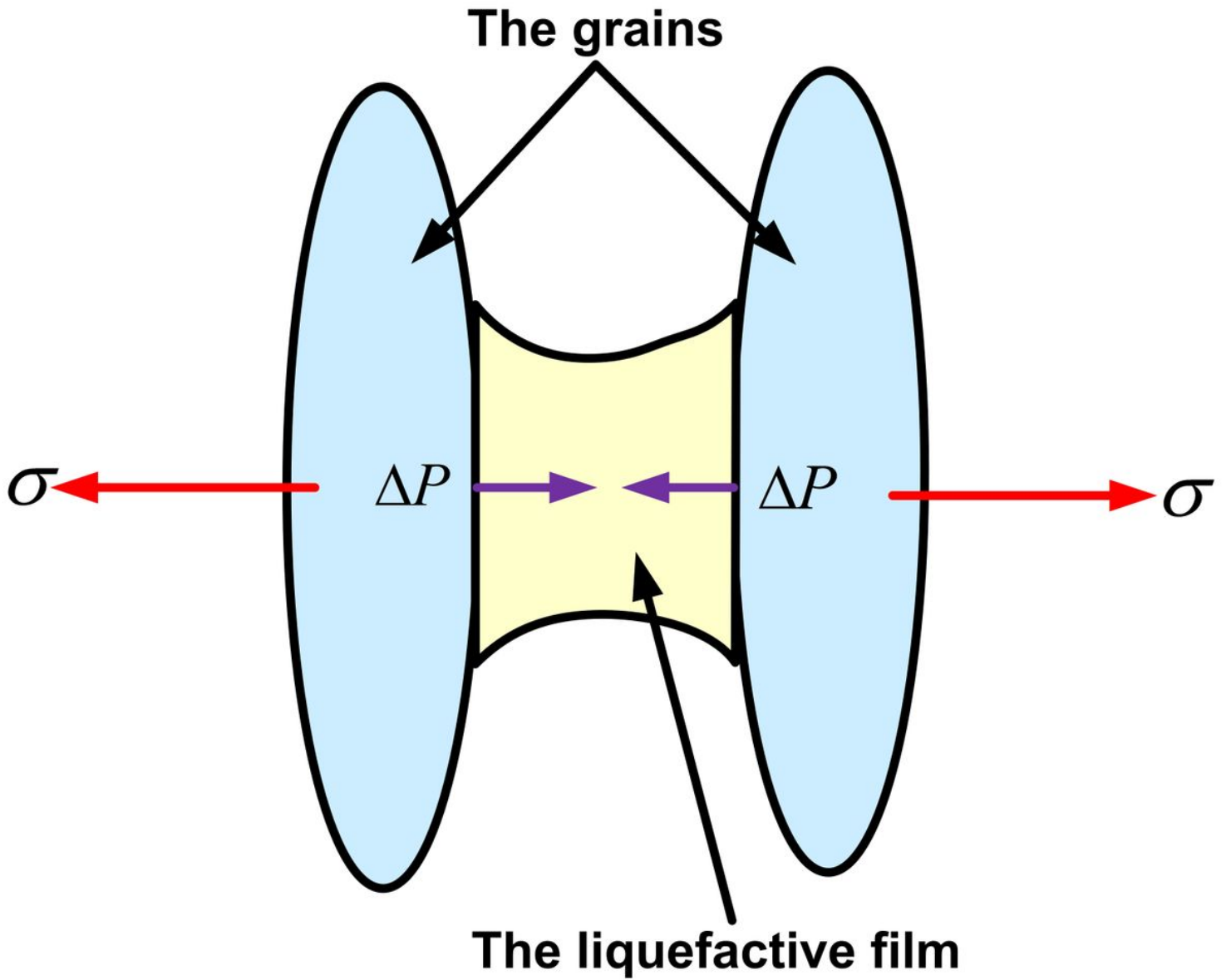


Figure 11

A schematic diagram of liquid film cracking mechanism [34].

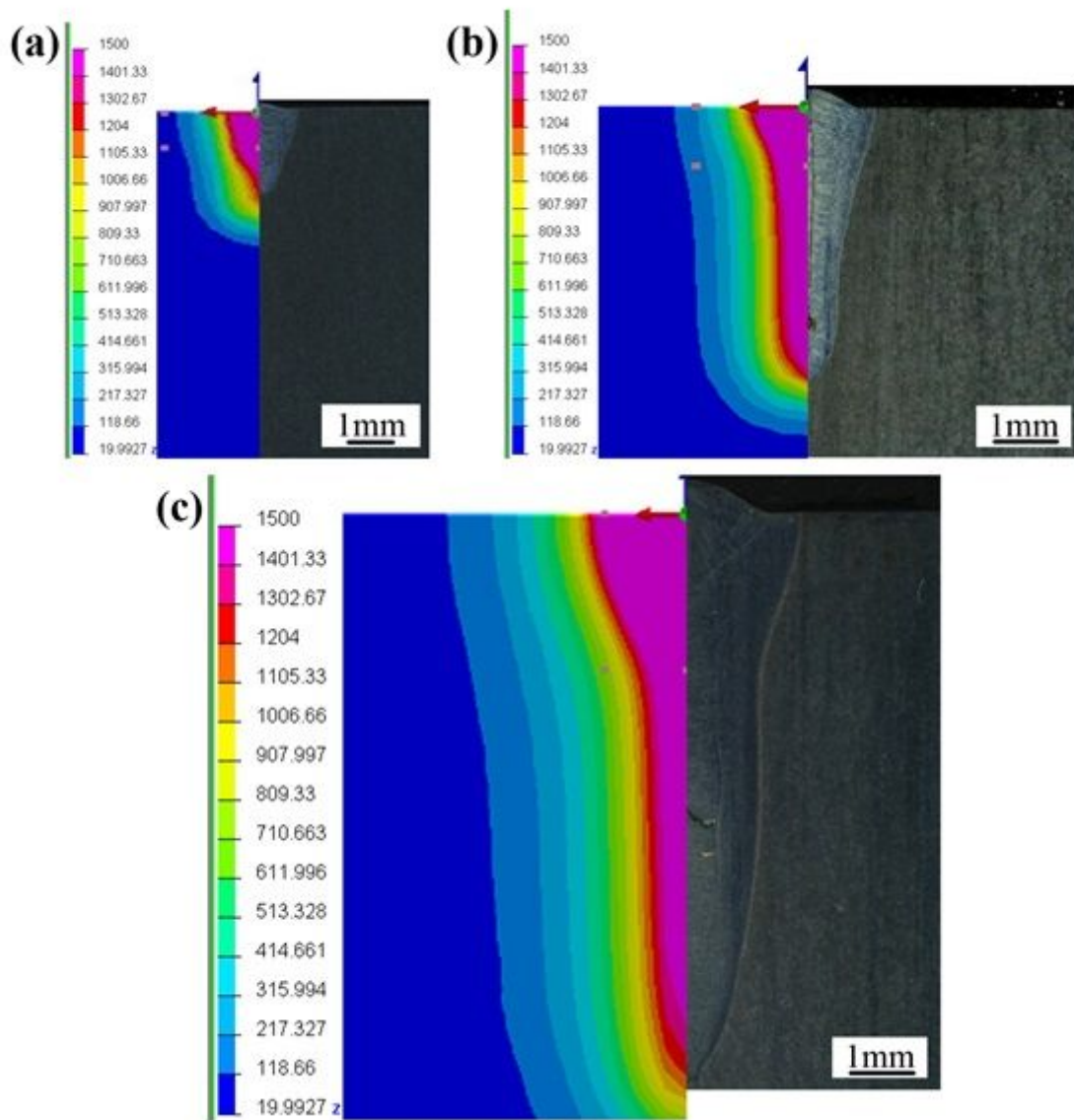


Figure 12

Comparison in overall size between simulation model and macro morphology in (a) L-1; (b) L-3; (c) L-4. Among them, the left half and the right half of each image (a, b and c) is the temperature field and the macro morphology, respectively.

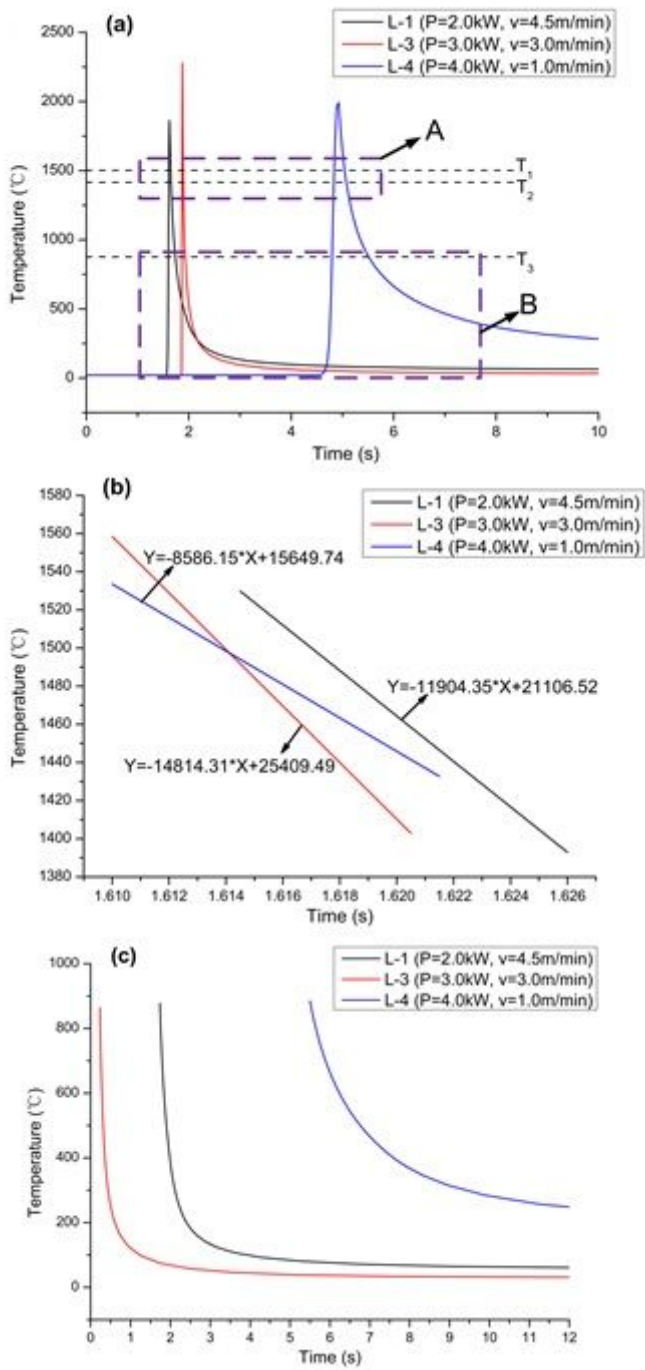


Figure 13

(a) curve of thermal cycle in L-1, L-3, and L-4; (b) the magnification of region A; (c) the magnification of region B.

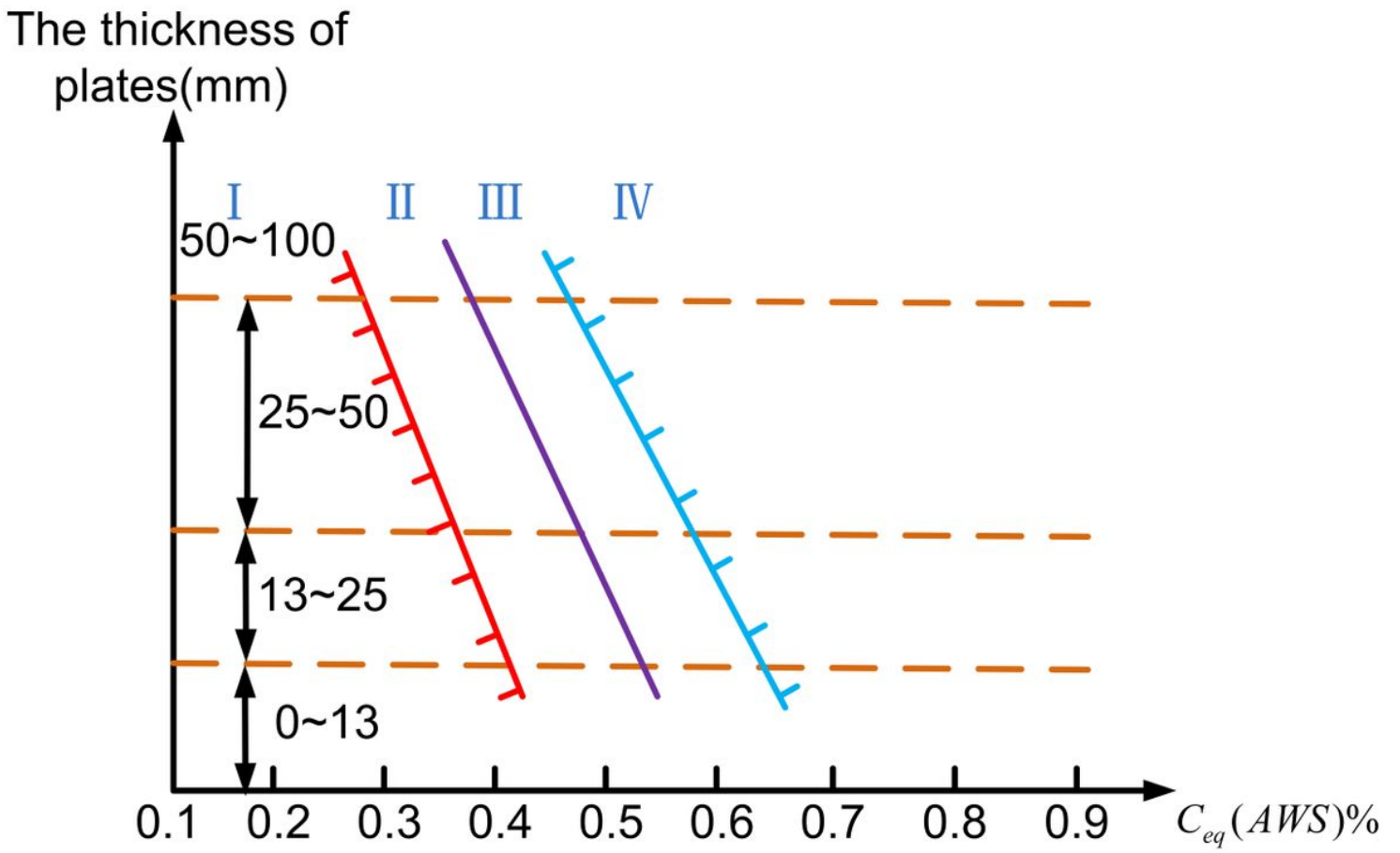


Figure 14

Grade of welding properties of steels [39]. ☒: Excellent ☒: Good ☒: Quality ☒: Poor

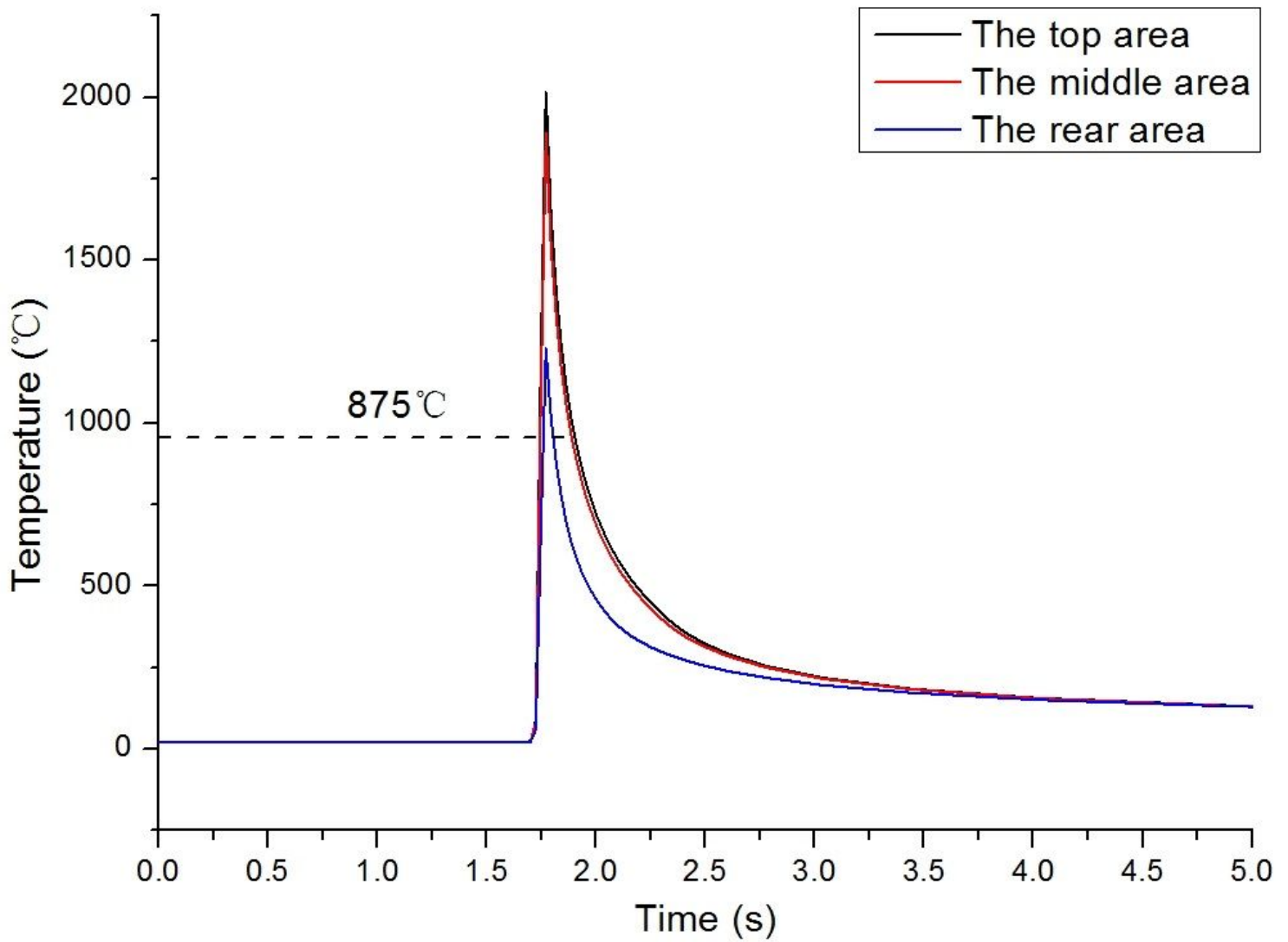


Figure 15

Curve of thermal cycle in L-3 in different zones.

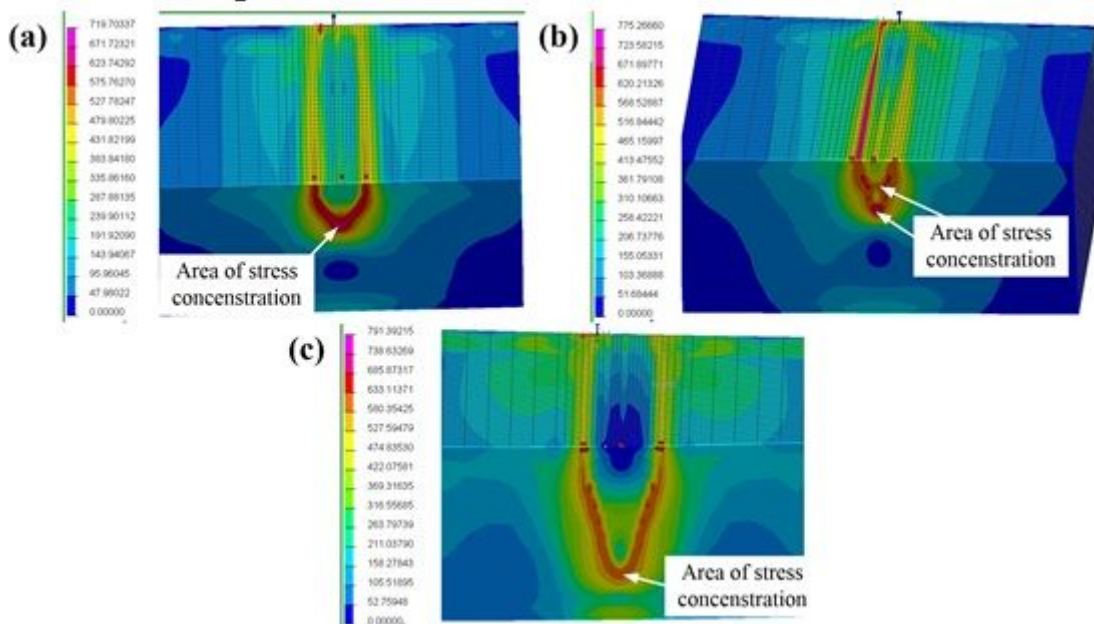


Figure 16

Distribution of the stress field in (a) L-1; (b) L-3; (c) L-4.

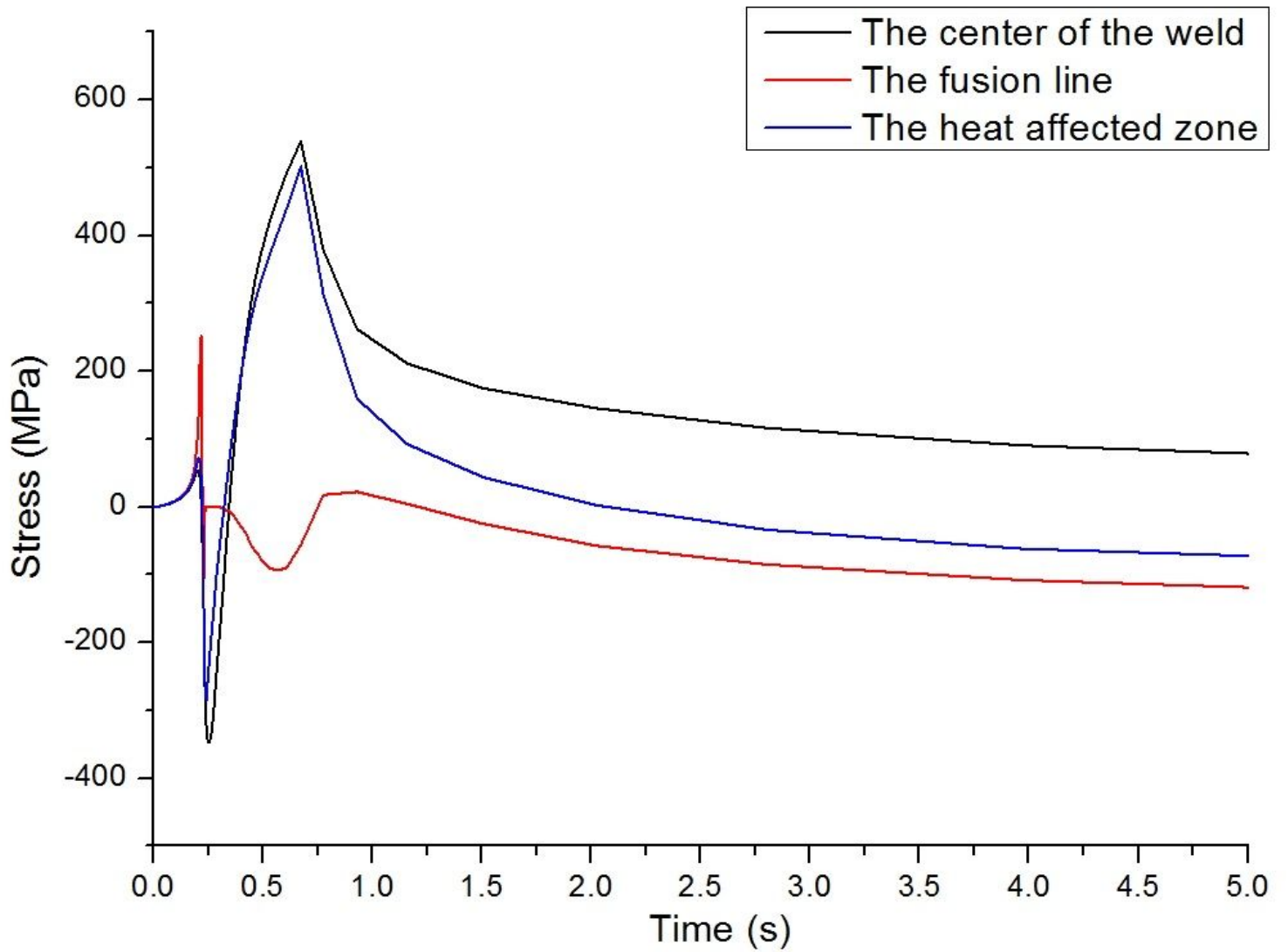


Figure 17

Curve of stress cycle in L-3.